NASA Dragonfly Mission – Rotor Blade Design and Optimization

Sven Schmitz
Boeing/A.D. Welliver Professor
Dept. of Aerospace Engineering
The Pennsylvania State University
University Park, PA 16802

Kate Gruber
Aeronautical Engineer Sr
Sikorsky, A Lockheed Martin Company
Stratford, CT 06615

Jason Cornelius
Aerospace Engineer
Aeromechanics Office
NASA Ames Research Center
Moffet Field, CA 94035

Gracelyne Allred
Graduate Student Researcher
Dept. of Aerospace Engineering
The Pennsylvania State University
University Park, PA 16802

Felipe Ruiz
Rotors Mechanical Lead
Johns Hopkins University Applied Physics Laboratory
Laurel, MD 20723

Patrick Bowles
Computational Aero Manager
Sikorsky, A Lockheed Martin Company
Stratford, CT 06615

Ramin Modarres
Senior Staff Dynamics Engineer
Sikorsky, A Lockheed Martin Company
Stratford, CT 06615

Peter Lorber
Lockheed Martin Fellow
Sikorsky, A Lockheed Martin Company
Stratford, CT 06615

ABSTRACT

The objective of NASA's 4th New Frontiers Mission, *Dragonfly*, is to explore the surface chemistry and habitability of Saturn's largest moon, Titan. With its thick nitrogen atmosphere, liquid methane cycle, and rich, organic surface materials, Titan holds clues to prebiotic chemistry to answer fundamental scientific questions about the building blocks of life. The combination of high fluid density (4.4x) and low gravity (1/7th) compared to Earth makes exploration of this cryogenic ocean world in the outer solar system feasible by means of a relocatable lander - this is *Dragonfly*, a multi-rotor vehicle designed for the unique atmospheric conditions and environment at Titan. *Dragonfly* enables flight in a quad-rotor configuration with two counter-rotating, canted rotors mounted on each of four sting arms. All eight rotors are three-bladed, stiff metal rotors that are controlled by variable-speed electric motors. The objective of this paper is to tell the story of *Dragonfly's* rotor blade design and optimization, starting with the conceptual design based on flight requirements for Titan, preliminary design iterations of the rotor blades, and detailed design and optimization of the final configuration. Details are given with respect to design constraints driven by the cryogenic Titan environment, resulting from scientific instruments located on *Dragonfly*, and the overall mission flight profile. Design tools ranged from momentum theory to free-wake methods, hybrid computational fluid dynamics (CFD), and blade-resolved CFD analyses compared to wind tunnel measurements of rotor and lander combinations.

NOTATION

A	Rotor Swept Disk Area [m^2]
a	Speed of Sound [m/s]
C_T	Rotor Thrust Coefficient, Thrust/(ρAV_{Tip}^2)
C_Q	Rotor Torque Coefficient, Torque/(ρAV_{Tip}^3 R)
c_r	Local chord length [m]
FM	Figure of Merit, $C_T^{3/2}/\sqrt{2}C_Q$
F_i	Rotor Hub Forces, F_x, F_y, F_z
g	Gravitational Acceleration [m/s^2]
M_i	Rotor Hub Moments, M_x, M_y, M_z
Ma	Freestream Mach Number, V_∞/a
Re	Local Reynolds Number, $\Omega r c_r/\nu$
R	Rotor Blade Radius [m]
r	Radial Position Along Blade [m]
SA	Shaft Angle, between free-stream and rotor disk
V	Wind Tunnel Speed [m/s]
V_{Tip}	Blade Tip Speed, ΩR [m/s]
V_x	Rotor Edgewise (Forward) Speed, $V * \cos(SA)$
ρ	Density [kg/m^3]
ν	Kinematic Viscosity [m^2/s]
σ	Thrust-Weighted Rotor Solidity
Ω	Rotor Rotational Velocity [rad/s]
μ_x	Rotor Advance Ratio Parallel to Rotor Disk, $(\cos(SA) * V_\infty)\ /(\Omega\ R)$

ACRONYMS

BEMT	Blade Element Momentum Theory
CAD	Computer Aided Design
CFD	Computational Fluid Dynamics
CLS	Closed-Loop Simulation
EXP	Experimental (TDT Data)
HEEDS	Hierarchical Evolutionary Engineering Design System
HG	Heavy Gas (i.e. R-134a in TDT facility)
NASA	National Aeronautics and Space Administration
rpm	Revolutions per Minute
TDT	Transonic Dynamics Tunnel
VDM	Virtual Disk Method

INTRODUCTION

Discovered in 1655 by Dutch astronomer Christian Huygens, Saturn's largest moon Titan remained a mysterious world with a hazy atmosphere until the Voyager flybys of 1980-

Presented at the Vertical Flight Society's 82nd Annual Forum & Technology Display, West Palm Beach, FL, USA, May 5-7, 2026.

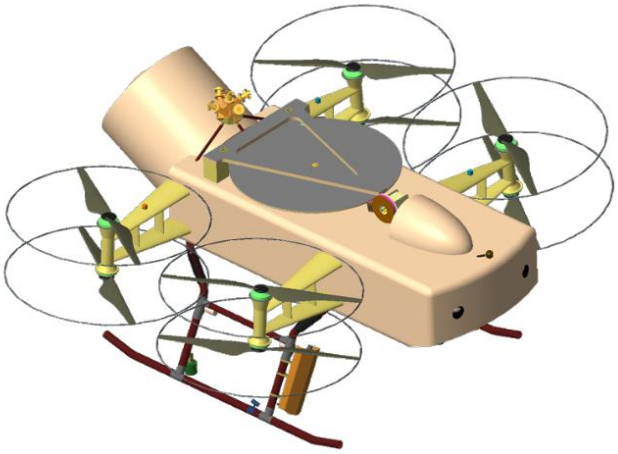
This is a work of the U.S. Government and is not subject to copyright protection in the U.S.

1981. Since then, Titan has become one of the most interesting planetary bodies in the solar system for future exploration, Refs. 1-2. In 2005, the Huygens probe separated from the Cassini mission orbiter and descended through the atmosphere onto Titan's surface. A wealth of scientific questions have since been asked about Titan's prebiotic chemistry and habitability in comparison to an early Earth circa 4 billion years ago. With its thick (4x Earth) Nitrogen atmosphere and cryogenic surface temperature (approx. 90K), the low-gravity (1/7th Earth) Titan environment may harbor important clues to the formation of early life here on Earth, Refs. 3-4.

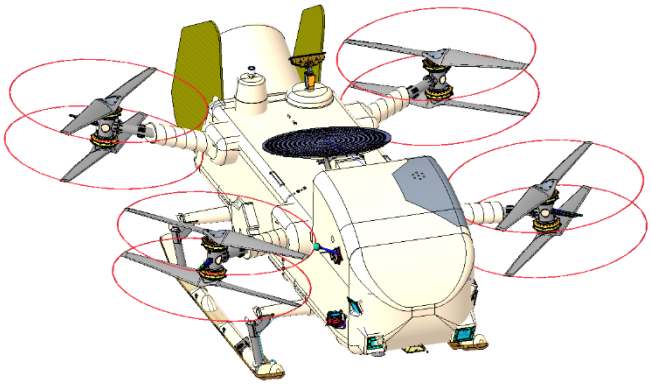
In 2019, Titan's future scientific exploration was spurred by NASA awarding its 4th New Frontiers Mission to *Dragonfly*, a multi-rotor relocatable lander, Ref. 5. *Dragonfly* is equipped with a multitude of scientific instruments to investigate, among other scientific objectives, Titan's surface chemistry and habitability as an ocean world with abundant carbon-rich chemistry. The combination of Titan's low gravity and thick atmosphere enable the *Dragonfly* lander being designed as a multi-rotor vehicle powered by a multi-mission radioisotope thermoelectric generator (MMRTG). The mission is scheduled to launch in 2028, and following an Earth gravity assist, expected to arrive at Titan in late 2034. Figure 1 shows a snapshot of the evolution of the *Dragonfly* lander configuration, from the early concept stage Phase A to Mission Preliminary Design Review (PDR), and Mission Critical Design Review (CDR), Ref. 6.

The dimensions of the *Dragonfly* lander are that of a small-size car, with an approximate body length of 4m and maximum rotor tip spacing of 3.8m on opposite (left to right) sides of the body. These dimensions are driven by the size of the aeroshell in which *Dragonfly* is housed during its journey to Titan. Indeed, the MMRTG, seen as the cylinder in Figure 1 at the back of the lander, is set at a specific angle, and it is required to be installed last when the vehicle is already stowed in the aeroshell on top of the launch system. Upon arrival at Titan, the *Dragonfly* lander is released from the capsule's backshell after the preparation to powered flight (PPF) sequence, enters the transition to powered flight (TPF) maneuver with full rotor control, and then searches for a safe landing site before setting down on Titan's surface, see Refs. 4,7. The quad-rotor configuration was chosen early in Phase A as the configuration that maximizes overall rotor disk area. Some of the early configuration studies are summarized in Refs. 8-10. More recent descriptions are in Refs. 11-13.

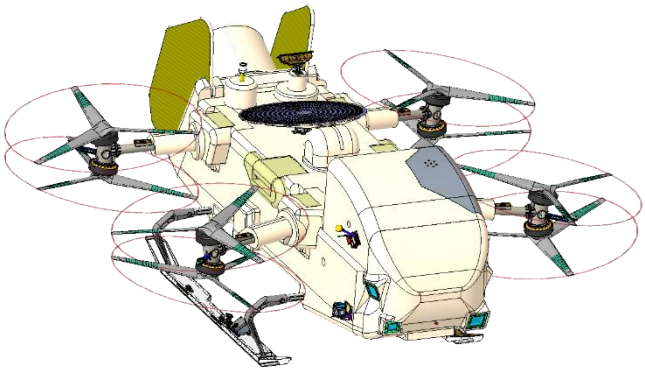
Some of the notable changes to the lander body from Phase A to Phases B and C of mission development are various aerodynamic and thermal features that became necessary. Large fins (shown in green in Figure 1) were installed alongside the MMRTG for enhanced yaw stability. The lander body itself was reshaped significantly to be able to house a number of scientific instruments; in particular, the nose was reshaped to accommodate requirements for camera view and aerodynamic drag reduction. Also, the folding mechanism of the low-gain antenna was changed such that the low-gain



(a) Concept Phase A (2017-2019)
2-Bladed Coaxial, Counter-Rotating Rotors (No cant)



(b) Mission PDR Configuration (Phase B, B*, 2019-2023)
2-Bladed Coaxial, Counter-Rotating Rotors (Canted)



(c) Lander CDR Configuration (Phase C, 2025-)
3-Bladed Opposite-Canted, Counter-Rotating Rotors

Figure 1. NASA Dragonfly Lander.

antenna rests in an approximate streamline position behind the front body section, thereby again reducing aerodynamic

body drag. Between the Mission PDR and Lander CDR configurations, the body fuselage was widened to comply with thermal requirements of variable temperature zones inside the lander body, see also Ref. 14.

As for the *Dragonfly* lander's rotor design, it progressed from its two-bladed Phase A planform design in 2017 to a robust, multi-role, three-bladed design with simpler planform in 2025. From the Concept Phase A to Mission PDR configuration, the fore-aft spacing between rotors on a given lander side was increased by shortening blade length by about half an inch and setting the rotor sting arm at a cant angle. This allowed additional fore-aft spacing and associated tip clearance between adjacent rotors and increased both yaw and pitch control authority. Another notable configuration change occurred between Mission PDR and Lander CDR. Here, increased nominal rotor thrust as a direct result of increased lander mass resulted in additional vibratory loads due to the two-bladed rotor system that were difficult to divert from affected instruments. A number of active and passive concepts were explored to reduce vibrations with careful consideration of complexity, space, and mass requirements. This ultimately prompted the change to a three-bladed rotor configuration, see Figure 1 bottom. In addition, controlling primarily lander yaw attitude during the Preparation to Powered Flight (PPF) maneuver, see Ref. 13, necessitated arranging the three-bladed rotors with opposite cant. The final rotor design, which passed *Dragonfly*'s Critical Design Review in March of 2025, uses brushless DC motors driving four pairs of counter-rotating rotors where the rotor-pairs are positioned in a quad-copter, "X" arrangement. The constant-pitch, speed-controlled vehicle positions the upper and lower rotors on each arm at cant angles to deliver the required lift and control authority. *Dragonfly* must fly through many conditions and avoid Vortex Ring State (VRS). This requires the rotor design to be robust across the entire rotor aerodynamic flight regime.

The objective of the present paper is to describe the general evolving requirements that drove the rotor design between 2017 and 2025 and its final maturation towards Lander CDR. An overview of the rotor planforms is shown in Figure 2, labeled by key program phases. All rotor planforms shown in Figure 2 are based on a two-bladed coaxial rotor pair.

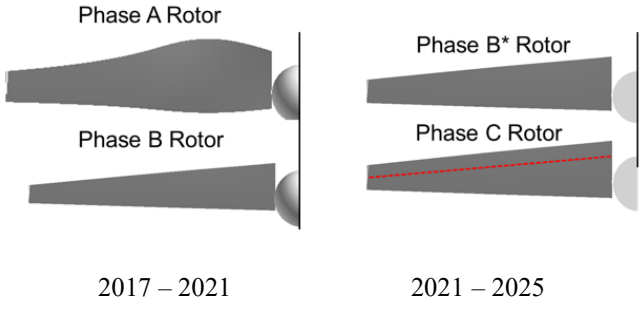


Figure 2. Evolution of Dragonfly Rotor Blade Planform, Phase A-C (2017-2025).

Note that the 'red' line on the Phase C rotor planform indicates the equivalent three-bladed Phase C planform where each blade is 2/3rd the chord of the two-bladed baseline, thereby keeping constant rotor solidity.

The paper is organized as follows: The section 'Rotorcraft Flight on Titan' provides a brief introduction of Titan atmospheric conditions and sets *Dragonfly* flight at Titan in perspective to general rotorcraft flight on Earth. Furthermore, this section includes some momentum-theory considerations of basic rotor design parameters and performance metrics. Following, the section 'Design & Analysis Tools' introduces the various computational tools at various fidelity levels used to analyze and improve the *Dragonfly* rotor design. The section on 'Conceptual Design' focuses on the early Phase A design and associated lessons learned. Next, the section on 'Preliminary Design' features the Phase B and the later Phase B* rotor as a direct result of structural and vibratory constraints. In addition, a subsection focuses on the two-bladed Phase C rotor which was a result of a systematic design optimization study to reduce the total energy required over a leapfrog mission profile. The subsequent section on 'Detailed Design' features detailed analyses of possible performance improvements beyond the three-bladed Phase C rotor and the role of the design and analysis tools used as part of this effort. Next, a section on 'Rotor Manufacturing Process' provides specifics on machining the stiff metal rotors for wind-tunnel testing and ultimately for the *Dragonfly* lander. Towards the end of the paper, a section on 'Experimental Validation' describes relevant wind-tunnel test campaigns in the NASA Langley Transonic Dynamics Tunnel (TDT), named TDT-1 and TDT-2A, conducted in Phase B and Phase C of the program. Here the objective is focused on maturing predictive capability of the analysis tools and resulting confidence to predict rotor performance of the final three-bladed Phase C rotor at Titan. At the end of the paper, the section 'Conclusions' provides an executive summary of *Dragonfly* rotor design and optimization.

ROTORCRAFT FLIGHT ON TITAN

In general, Titan is a suitable environment for vertical flight. This is primarily driven by Titan's low gravity (1/7th of Earth) and high fluid density (4.4x Earth). Furthermore, cryogenic temperatures on Titan result in a low fluid kinematic viscosity (1/12th of Earth) and consequently fairly high chord-based Reynolds numbers on rotor blades. All of this allows a full-size *Dragonfly* lander to take battery-powered flight on this ocean world a billion miles away from Earth. Table 1 summarizes some key approximate performance limits for the octocopter type configurations shown in Figure 1. With a total mass and projected footprint close to that of a small helicopter on Earth, the *Dragonfly* lander only weighs about as much as a small motorcycle on Titan.

Distributing the thrust load over four rotor pairs each having a disk area similar to the Mars Ingenuity helicopter, see Refs. 15-19, the resulting downwash in hover on Titan is fairly low,

owing to the relatively low disk loading and high fluid density. The low disk loading and hover downwash require careful blade design for fixed-pitch speed-controlled rotors in order to avoid blade stall in descent and to avoid VRS conditions possible at relatively low descent speeds.

Table 1. Rotorcraft Flight on Titan (Phase C).

Titan Conditions	
Surface Temp. [K]	94
g [m/s^2]	1.32
ρ [kg/m^3]	5.4
ν [m^2/s]	1.23E-06
a [m/s]	195
Dragonfly Lander	m = 995kg
<u>*Dragonfly* Rotor Pair</u>	
Max. Thrust [N]	335
Radius [m]	0.675
Hover Downwash [m/s]	4.6
Tip Speed [m/s]	51 (723rpm)
Tip Mach Number	0.26
Reynolds Number Re_{75}	3.0E+06
Thrust Coefficient	0.0166
Power Coefficient	0.00156
Hover FM	0.77
Disk Loading [Pa]	235
Power Loading [N/kW]	210
Max. Range Speed [m/s]	9
Advance Ratio	0.14
Rotor L/D$_e$	2.5 – 3.0

In terms of required blade tip speed and Reynolds number, *Dragonfly* rotor blades operate in a Reynolds and Mach regime typical of utility-scale wind turbines on Earth, see Ref. 4, with tip Mach numbers around 0.3 and chord-based Reynolds numbers of order 3.0*10^6, resulting in a good hover figure-of-merit. Even at highest rotor speeds in climb, maximum tip Mach numbers are only weakly subsonic compressible, though this has to be taken into account for C81 table generation. The power loading of *Dragonfly* rotors is quite high, thanks once more due to low gravity and high fluid density of the Titan environment, see Table 1.

This in turn allows rotors to be driven by battery-powered electric motors. As far as the speed for maximum range is concerned, it is also fairly low for a vehicle that size and is a consequence of high equivalent flat-plate drag area of the lander body and resulting fast rising parasite power in forward flight in the thick Titan atmosphere (Ref. 4). Consequently, the relatively low cruise speed leads to a maximum rotor L/D$_e$ in forward flight of only about 2.5 – 3.0 at most. Figure 3 shows the *Dragonfly* lander on a power loading versus disk loading graph adapted from Ref. 20. It is interesting to see in Figure 3 that *Dragonfly* essentially operates in a gap seen between Earth-based large-scale and micro-scale rotors, i.e. where current Unmanned Aerial Systems (UAS) are developed for missions on Earth.

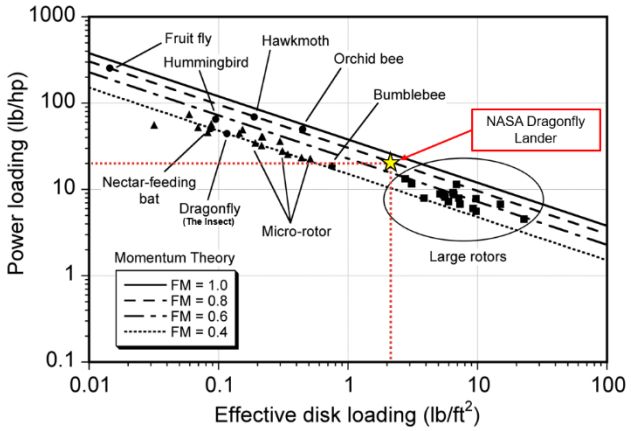


Figure 3. Vertical Flight - Power loading vs. thrust loading, adapted from Ref. 20.

Basic Momentum Theory Considerations

The three most stringent requirements for *Dragonfly* rotors include i) hover thrust from Table 1, ii) requirement of stiff metal rotor blades to be manufactured with contemporary technology for the cryogenic Titan environment, and iii) feasible motor torque and speed that can be supplied by sizable direct-drive electric motors at Titan. The design space around these three basic requirements can be explored using simple momentum-theory relations. Recasting the definition of rotor thrust coefficient, $C_T = T/\left(\rho A V_{Tip}^2\right)$, to solve for rotor tip speed, and combining with a classical relation in hover writing thrust coefficient in terms of mean lift coefficient and thrust-weighted solidity, $C_T/\sigma = \bar{c}_l/6$, one can estimate rotor figure-of-merit, rotor speed, and rotor torque for given thrust and disk area as a function of thrust-weighted solidity and mean lift coefficient.

From a power perspective, reducing tip speed and hence profile power to the extent possible is desirable. This drives both rotor solidity and mean lift coefficient to higher values. Indeed, a classical argument for best hover performance drives the choice of the mean lift coefficient to maximize $c_l^{3/2}/c_{d0}$ where c_{d0} is the mean profile drag coefficient. For standard, Earth-based, fixed-speed, and pitch-controlled helicopter rotors, this results in mean lift coefficients of around 0.7 with sufficient stall margin. In contrast, stiff variable-speed, fixed-pitch rotors operating in the Titan environment are prone to stall during descent due to reduced inflow (and hence higher angles of attack) caused both by reduced rotor speed for trimmed thrust and upwash through the rotor due to the descent speed. This by itself sets the mean lift coefficient for *Dragonfly* rotors lower at around 0.5. A higher rotor solidity supports the requirement of stiff blades and good hover performance at lower tip speed, though it can result in both high rotor torque and higher advance ratio in forward flight, with consequent notable increase in hub vibratory levels of the stiff rotor system.

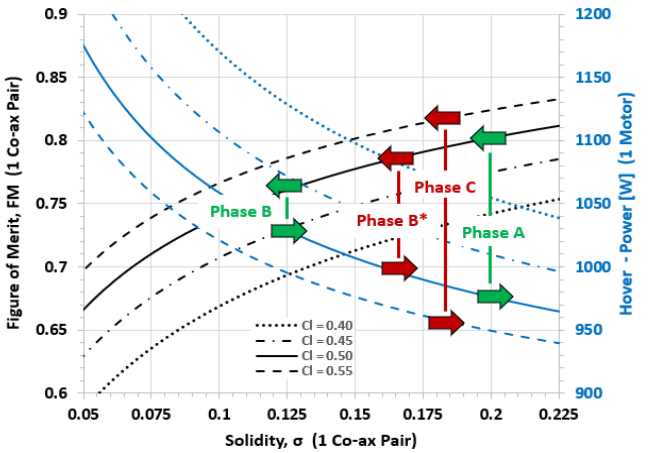
Consequently, both rotor mean lift coefficient and rotor solidity are two important early design considerations that follow through with subsequent iterations of rotor hub vibrations in forward flight, airfoil choice, manufacturing process, and resulting rotor mass (and rotor inertia) with their effect on rotor control margins and lander mass.

Figure 4 attempts to capture some of the trade space of rotor mean lift coefficient and rotor solidity and their effect on hover figure-of-merit, cruise advance ratio, motor power, torque, and rotor speed. Note in Figure 4 that rotor solidity is shown on the horizontal axis, while several curves capture a suitable range of mean lift coefficients for the *Dragonfly* rotors. All rotor planforms shown earlier in Figure 2 are captured, with the direction of arrows indicating the relevant vertical axis, i.e. black curves pointing left and blue curves pointing right. Values shown in Figure 4 are not exact with respect to later detailed designs but represent 'delta' values in conceptual momentum-theory analyses.

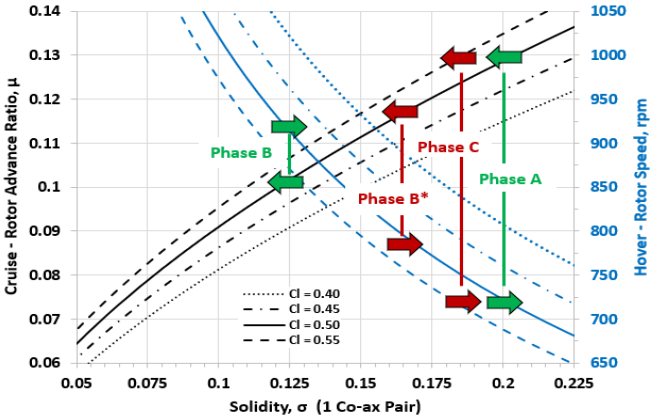
In Figure 4, Phase A and Phase B rotors are shown in green, while Phase B* and Phase C are shown in red. This is to emphasize that Phase B* and Phase C rotor planforms are closed *Dragonfly* rotor designs that satisfy all subsequent analyses in aeromechanics, control, manufacturing, and vehicle mass balance. Later sections in this paper will describe in more detail the reasons as to why Phase A and Phase B designs violated more than one rotor system requirement. From a broad perspective, the Phase A and Phase B designs bound the feasible range for *Dragonfly* rotor solidity. The Phase B* design is practically in the middle of that range, with the Phase C design pushing to slightly higher mean lift coefficient and rotor solidity, and hence rotor performance in terms of figure-of-merit, made possible through the various lessons learned and evolving requirements in design and analysis iterations throughout the mission development.

In addition to other aspects, Figure 4a shows that the Phase C rotor exhibits about two counts in figure-of-merit improvement compared to the closed Phase B* design. Note that the resulting approx. 20W less in hover power for one motor cascades to an appreciable effect on energy use during a typical leapfrog flight as will be shown in a later section. Figure 4b demonstrates that the Phase C rotor has practically the same advance ratio in forward flight as the Phase A rotor, and higher than the closed Phase B* rotor design. This was possible due to both adjustments in blade stiffness and the ultimate transition to a three-bladed rotor system for Phase C. Figure 4c in turn shows that motor torque is practically the same for Phase A and Phase C rotors, a result of respective delta values in mean lift coefficient and rotor solidity. The delta in motor torque (in hover) between the closed Phase B* design and the final Phase C rotor is exactly 1Nm and a result of a feasible constraint set by the motor development stage at the time, see later section.

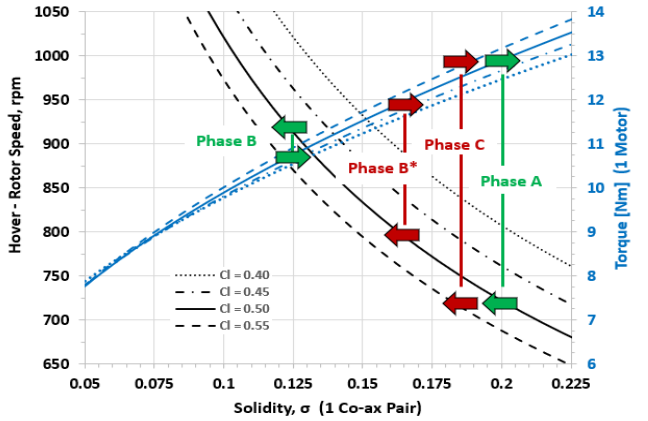
Table 2 shows examples of basic Phase C rotor performance in terms of power, speed, and torque per direct-drive electric motor. Note that these are estimates from momentum theory and not actual Phase C values.



(a) Hover FM and Power.



(b) Cruise advance ratio and Hover rotor speed.



(c) Hover rotor speed and motor torque.

Figure 4. *Dragonfly* Rotor Basic Momentum-Theory considerations and design parameters, Phases A-C.

Table 2. Basic Phase C rotor performance. (Momentum Theory)

Nominal Condition	$m = 995kg$, $c_l = 0.55$, $\sigma = 0.185$		
1 Motor	Hover	2m/s vert.	1g lat.
Power [W]	956.0	1183.9	2146.6
Rotor Speed [rpm]	716	776	852
Torque [Nm]	12.75	14.55	24.09

Motor-Out Cond.	$m = 995kg$, $c_l = 0.55$, $\sigma = 0.185$		
1 Motor	Hover	1m/s vert.	0.5g lat.
Power [W]	2173.4	2419.0	2569.2
Rotor Speed [rpm]	914	963	966
Torque [Nm]	22.71	24.00	25.40

The upper part of Table 2 refers to the nominal condition of a coaxial rotor pair and documents values for one motor. In addition to hover, a 2m/s vertical climb is considered along with a 1g lateral maneuver at 45deg bank angle. As for the lower part of Table 2, here the case of a motor-out condition is considered where only one rotor (of a given rotor pair) provides the full required trimmed thrust. Note here that vertical climb is reduced to 1m/s and the lateral maneuver to 0.5g at 30deg bank angle. These types of momentum-theory analyses as shown in Figure 4 and Table 2 were valuable throughout Phases A-C in providing good estimates and requirements for parallel developments of electric motors and closed-loop simulation (CLS) of *Dragonfly* flight on Titan.

DESIGN TOOLS

This section provides short descriptions of the various tools used to design the *Dragonfly* rotors. Cross-tool comparisons are a key component of *Dragonfly*'s engineering, with analyses across multiple tools and organizations providing confirmation of the validity of model setups and assumptions. As the program advanced, the fidelity of the tools also improved – the rotor's constrained design was well established using lower-fidelity methods, but high-fidelity CFD-CSD and full-vehicle CFD were used to provide confidence in the design at varied operating conditions.

Table 3 shows the range of aerodynamic modeling capability used across the program along with computational expense. Darker green items indicate the least complexity and smallest computational expense, typically used for earlier studies or analyses requiring a large number of analyses. As the fidelity and complexity increases, so does the computational expense, and so these types of analyses are reserved for spot-checks and cross-validation analysis of key flight conditions. The various tools discussed in the following sections all fit within this framework of model fidelity.

In regards to the computational tools described in the following section, computational times vary greatly across these tools and scale with fidelity, with Free Wake cases running in a matter of minutes, isolated Virtual Disk simulations completing in 1 hour, and installed Virtual Disk simulations completing in 12 hours on 10 nodes. For comparison, full-body Helios simulations require approximately 3-4 days on 20 nodes. Recent improvements in GPU capability aim to shorten the computational time significantly, with speedup times close to 10x at this stage.

Table 3. Fidelity of Model Components for Various Design Tools and Use Cases.

External Flow Field Equations Solved	Turbulence Model	Rotor Model	Airframe	Aero Interactions
Steady NS	Steady RANS	Uniform steady actuator disk	Idealized	Building block approach (none)
Unsteady NS or iNS-L	Unsteady URANS	Space-variable, time-averaged disk (BEMT)	Minimal idealization	Spatial average BEMT and rigid airframe
Unsteady NS, Real Gas Equations	DES	Rotating lifting lines or momentum sources	Minimal idealization + structural model	Blade passage and wake interactions, rigid airframe
	WMLES	Rotating blade-resolved (rigid)		Unsteady aero loads at cg, coupled to FEA modal model
	LES / DNS	Rotating blades + structural model		Apply unsteady aero at structural model locations

Least Capability	Moderate Capability	Current High Capability	In Development	Future Ideal

Increasing complexity and computational expense

C81 Table Generation

Airfoil tables play a central role for all design and analysis tools used on the *Dragonfly* program. C81 tables were generated upfront and disseminated to various teams using different design tools to maintain consistency across the program. During Phase A and early Phase B, tables were primarily generated using Xfoil and ARC2D; however, the evolution of the rotor design to thicker airfoils necessitated using OVERFLOW. Therefore, all C81 tables used in the various tools were generated using OVERFLOW (Ref. 21) with Spalart-Almaras turbulence modeling for wind-tunnel test conditions and actual conditions at Titan. Either AFTGen or Pointwise was used to create the 2D O-Grid, as shown in Figure 5, with a y+ target of 1 at maximum Mach number for each airfoil. Figure 6 shows examples of C81 lift curves along the Phase B* rotor blade.

The methodology described here for C81 table generation was used throughout the *Dragonfly* program phases to compute conditions expected at Titan as well as in the various wind tunnel test campaigns described in a later section.



Figure 5. O-Grid around NACA 4412 airfoil with close-up of trailing edge, adapted from Ref. 22.

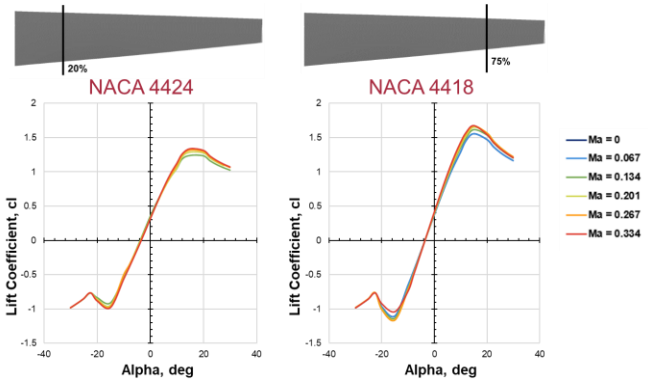


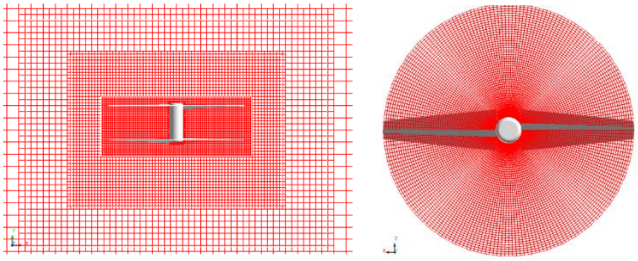
Figure 6. Example of Phase B* rotor NACA 4-series airfoil sectional lift curves from C81 tables.

RotCFD Virtual Disk Model

The RotCFD program uses a hybrid Blade Element Momentum Theory and Unsteady Reynolds-Averaged Navier-Stokes (BEMT-URANS) methodology. This means in particular that a URANS CFD solver computes the inflow and wake to a Virtual Disk Model (VDM) representation. The VDM interrogates local blade-section C81 airfoil tables akin to a BEMT method, see Refs. 23-26. As such a VDM can be considered a mid-fidelity approach between low-fidelity BEMT and high-fidelity blade-resolved URANS CFD, with a computational cost an order of magnitude less than a high-fidelity method. This enables the computation of hundreds of cases in a rotor performance matrix at good accuracy of time-averaged integrated forces and moments on the rotor disk at a reasonable computational cost. Figure 7 shows a coaxial rotor system embedded in tetrahedral body-fitted cells.

This setup also allows inclusion of geometric features such as the shaft connection between rotors and the entire fuselage which are not boundary-layer resolved but capture their overall effect on the inflow to the VDM rotor representations.

The far-field boundary is typically set 10 rotor diameters in all directions with progressive grid coarsening towards the boundaries of the solution domain. Grid sensitivity studies concluded that 90 cells across the VDM are sufficient for performance coefficients to be within a couple percent, see Refs. 22, 25. In order to account for tip effects, a linear tip-loss model is used within the VDM starting at 85% radius. The outer incompressible URANS solver uses a SIMPLE-based finite-volume solution method with a two-equation k-ε turbulence model.



Side View Top View

Figure 7. Example RotCFD VDM Grid Assembly.

The RotCFD VDM was instrumental in the Phase B preliminary rotor design process. It was the primary method used for the CFD prediction accompanying the Phase B* rotor TDT-1 test in the NASA Langley Transonic Dynamics Tunnel in 2022 that anchored the VDM approach as the routine rotor performance evaluation tool for *Dragonfly*.

SAC-MFW

SAC-MFW is a Sikorsky proprietary Weissinger-L lifting-surface model for blade aerodynamics calculated using C81 tables, combined with full-span distorted free-wake modeling in both periodic and accurate time-marching mode. This lower-order model was primarily used for quick trade studies during preliminary design and for later optimization studies when fast evaluations of many designs were necessary.

STAR-CCM+ Virtual Disk Model

Siemens Digital Industries Simcenter STAR-CCM+ is a commercial multi-physics software package. A mid-fidelity CFD approach was developed with this tool, with a steady-state Reynolds Averaged Navier Stokes (RANS), Spalart-Almaras (SA) turbulence model, and a Virtual Disk Blade Element Momentum Theory (BEMT) model for the rotors, referred to as the Virtual Disk Model (VDM) herein. The combined methodology is denoted RANS-VDM. The RANS-VDM uses a second order, central differencing scheme with boundedness.

Similar to the RotCFD virtual disk model, the rotor properties are specified in the VDM as spanwise tables of chord, twist, and airfoils. C81 tables developed using the previously described process capture airfoil section Mach and Re attributes, and provide airfoil lift and drag properties.

The virtual disk resolution was set according to best practice, with 120 azimuthal bins and 40 radial bins with a stretch ratio of 0.95 to cluster the bins at the tip, for a total of 5600 BEM grid points per rotor. The momentum source terms at these grid points were then interpolated onto the CFD discrete volume grid, which had a mesh size set to achieve 5 volume

cells across the thickness and 150 cells across the diameter. An unstructured mesh was utilized.

A half-cosine tip loss correction function was applied to correct the lift force at the tip of the blade, as the BEMT cannot capture the loss of lift near the tip due to the formation of the trailing vortex. The radial starting point for the tip loss function was determined by analyzing the radial thrust distribution of discrete blade simulations in hover to determine the point at which the thrust begins to drop. This process-based method was followed for each rotor update. A value of 0.85 was utilized for the 2-bladed Phase B* rotor and 0.93 for the 3-bladed Phase C rotor design.

This mid-fidelity RANS-VDM modeling approach has been utilized to create the large aero databases required to model *Dragonfly*'s flight operations, Refs 27, 28, with over 2000 cases required to cover the operating range of the vehicle. Despite known limitations of the approach, good agreement has been found both with higher-fidelity analysis tools and comparisons with test data from the NFAC and TDT test campaigns, see later sections.

Discrete Blade Analyses in CFD

Discrete blade simulations are used to resolve the blade and to simulate effects of tip vortices and blade vortex interactions that cannot be captured by the mid-fidelity virtual disk approach. Two solvers are used for discrete blade analysis in CFD: Simcenter STAR-CCM+ and CREATE-AV Helios.

In STAR-CCM+, quadrilateral, anisotropic surface meshes with polyhedral near and far off-body discrete volume elements are utilized. Unstructured, overset meshes are used. An Improved Delayed Detached Eddy Simulation (IDDES) turbulence model is employed with second-order time discretization.

The CREATE-AV Helios multi-solver paradigm, Ref. 29, was utilized to perform high-fidelity CFD simulations. A structured CFD solver, OVERFLOW, was used to simulate the rotor blades, while an unstructured CFD solver, kCFD, was used for the rotor hub and lander body. The structured blade mesh and the unstructured hub mesh are shown in Figure 8. The off-body Cartesian mesh is shown in Figure 9. The finest level for the off-body mesh was 0.51 cm to allow for seamless oversetting with the rotor blade mesh and the hub mesh. The grid counts for the meshes are given in Table 4.

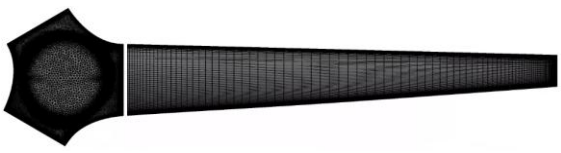


Figure 8. Helios structured blade mesh and unstructured hub mesh.

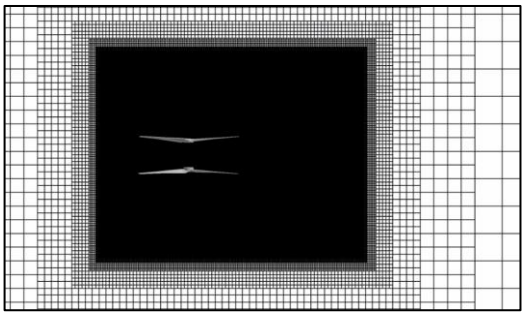


Figure 9. Helios Cartesian background mesh for isolated rotor pair configuration.

For the OVERFLOW solver, 4th-order central differencing, spatial discretization and 2nd-order time-marching schemes were used. The one-equation SA DDES turbulence model with rotational correction was used in OVERFLOW. The Helios native solver, SAMCART, was used for the background mesh with a 5th-order central differencing scheme and SA-DES turbulence model. The kCFD solver used SA-DDES turbulence model for the lander and rotor hub nearbodies. The simulations were performed with a quarter degree time step. Eight rotor revolutions were performed for forward flight cases and twelve revolutions for the hover cases.

Table 4. Helios Mesh Count.

OVERFLOW Rotor Mesh		
	Blade	201x100x90
	Root Cap	125x121x90
	Tip Cap	125x117x90
	Per Blade	1.8M
	Rotor Pair	11M
	Fore Aft Pair	22M
kCFD Hub Mesh		
	Single Hub	0.18M
	Rotor Pair	0.36M
	Fore Aft Pair	0.72
SAMCart Background Mesh		
	Background Mesh	517M

Full-Vehicle CFD

Full-Vehicle CFD models are used to include the effects of rotor-body interactions on rotor performance. Both virtual disk and discrete blade approaches can incorporate the lander body. CFD geometry for the lander body was prepared from as-designed CAD, retaining fine details in the geometry and minimizing idealization by leveraging the unstructured mesh capabilities of STAR-CCM+ and kCFD in Helios. Figure 10 shows an example of the lander body surface mesh and an up-close image of the volume and surface mesh of the arm, showing small features.

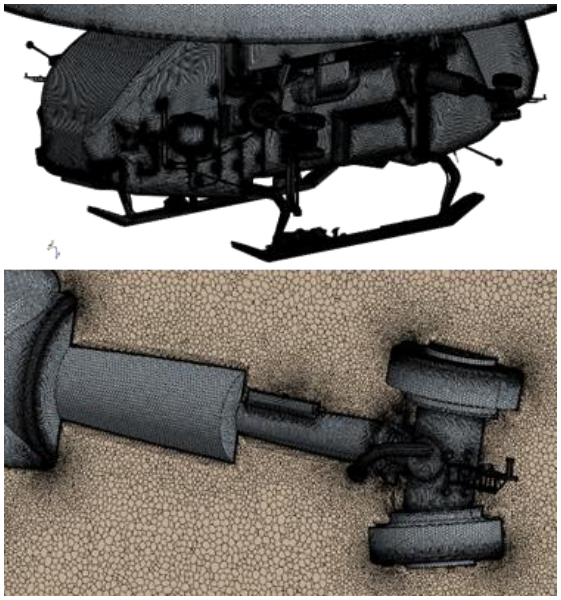


Figure 10. STAR-CCM+ Mesh with featured geometry.

RCAS

RCAS is a rotorcraft comprehensive aeroelastic analysis tool and uses a finite-element approach for modeling different rotorcraft configurations at varying levels of fidelity through an extensive library of structure, airloads, airwake, and aerodynamic interferences (Ref. 30).

RCAS-VVPM

The Viscous Vortex Particle Method (VVPM) is used, since it not only models the rotor wake dynamics, but also captures the rotor-to-rotor interferences. VVPM solves the incompressible Navier-Stokes equation in a vorticity-velocity form with a grid-free Lagrangian representation. The vortices are convected freely in the flow-field without any artificial dissipation. It also captures the physical wake distortion and diffusion due to air viscosity (Ref. 31). VVPM can easily be turned on as an inflow model within RCAS.

CFD-CSD

The highest level of fidelity, tightly-coupled Computational Fluid Dynamics (CFD) and Computational Structural Dynamics (CSD) employs the Helios and RCAS workflows to perform aeroelastic simulations, see Refs. 29-30.

CONCEPTUAL DESIGN

Conceptual Rotor Design - Phase A (2017-2019)

The most fundamental early design constraint is the requirement of *Dragonfly* having to fit within a given space capsule without any blade folding mechanisms. This requirement stemmed from early studies on mechanical complexity and weight penalty, in addition to the unprecedented challenges of folding mechanisms due to the cold temperatures of Titan's cryogenic environment. To optimize power loading of the *Dragonfly* lander, the approach led to maximizing rotor disk area. As seen in Figure 11, a two-bladed quad configuration does indeed maximize rotor disk area, and hence this configuration was chosen for all subsequent design iterations. Next, each station of the quad configuration was equipped with a set of two counter-rotating coaxial rotors, resulting in the original X-8 arrangement of the early concept *Dragonfly* lander, see Figure 1a.

As *Dragonfly* rotors had always been envisioned as stiff, fixed-pitch rotors driven by variable-speed electric motors, the X-8 configuration both enabled a single-fault tolerance (i.e. one motor-out condition) and resulted in larger torque margins for the anticipated electric motors because of distributing the loads between eight instead of four rotors. To fit into the aeroshell, it became clear that upper/lower rotor spacing in the coaxial X-8 configuration would be fairly close, i.e. not more than a quarter of the rotor diameter, which became another reason to necessitate rotor blades being structurally stiff. The conceptual Phase A blade planform design is also shown in Figure 11. Here, emphasis was given to a chord and twist distribution with good hover and climb performance using basic design relations from blade-element momentum theory of optimum twist and planform. Rotor performance during this early stage of the *Dragonfly* program was conducted primarily using BEMT methods and selected blade-resolved URANS computations of the coaxial system in hover using STAR-CCM+, see Ref. 32.

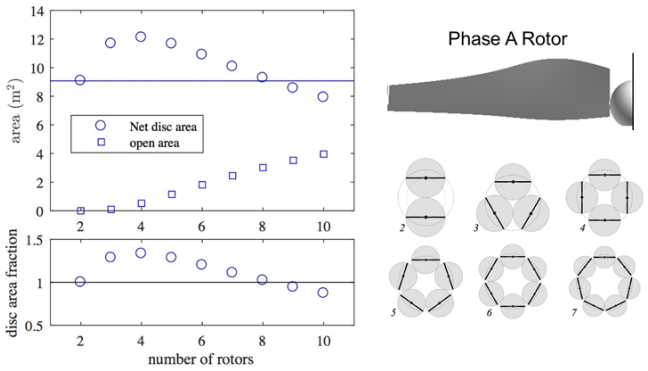


Figure 11. Phase A - Conceptual Study on Maximizing Rotor Disk Area, adapted from Ref. 8.

The planform had comparatively high solidity, see Figure 4, thereby minimizing blade tip speed and profile power. The Phase A rotor was equipped with thin rotorcraft airfoils. Towards the end of Phase A, with further conceptual studies on *Dragonfly* mobility and mission flight profiles becoming available, the relatively high solidity and consequent low tip speed resulted in an edgewise advance ratio in cruise that was subsequently regarded as too high with respect to hub vibrations of the stiff rotor system. In this context, it is important to note that *Dragonfly* maximum permissible lander mass in Phase A was actually less than half of that in late Phase B and Phase C, thereby leading to nearly twice as high of a cruise advance ratio in Phase A than shown in Figure 4b for the post-CDR *Dragonfly* lander.

Some additional lessons learned in Phase A were that the attribute of low pitching moment of conventional rotorcraft airfoils was not needed for a stiff rotor in edgewise flight. Furthermore, tip Mach numbers do not exceed 0.42 at Titan, i.e. no transonic flow is expected. Also, thin rotorcraft airfoils were not providing the required flap stiffness for the Phase A planform, and it became clear that a family of thicker airfoils would have to be chosen for Phase B. It also became apparent that higher rotor solidity would not be feasible to increase flap stiffness due to an emerging understanding of feasible torque-speed curves for direct-drive electric motors under concurrent Phase A development. As for the twist distribution with emphasis on hover and climb performance, it became apparent with the first rotor comprehensive analyses in descent that the Phase A rotor was very prone to stall, even at quite low descent speed. This was primarily driven by high blade twist in the inboard part of the blade.

The Phase A rotor demonstrated that designing a rotor for the *Dragonfly* lander to operate in the Titan environment challenged some of the conventional wisdom about Earth-based rotorcraft. The nature of the environment and emerging flight profiles to accomplish the *Dragonfly* science mission, alongside concurrent conceptual developments of subsystems such as electric motors and flight software, provided valuable insights towards Phase B rotor development.

PRELIMINARY DESIGN

In the preliminary design phase, a combination BEMT and RotCFD VDM analyses was used. Selected blade-resolved simulations were conducted using STAR-CCM+.

Dragonfly Phase B (2020-2021)

In Phase B, the primary rotor analysis tools used were RotCFD VDM for rotor performance and RCAS for blade dynamics and structural analysis. The Phase B rotor exhibited some notable deviations from the Phase A design. First, blade radius, and consequently disk area, were slightly reduced to provide sufficient tip clearance to the evolving *Dragonfly* main lander body. In order to reduce blade mass and inertia alongside cruise advance ratio and hence vibrations, the rotor solidity of the Phase B rotor was chosen to be notably smaller than that of the Phase A rotor, see Figure 2. The reduced rotor solidity also increased rotor speed, thereby reducing motor torque, cruise advance ratio, and hub vibrations. This came at the expense of reduced hover and climb performance, see Figure 4. To accommodate for the reduced performance, the Phase B rotor was equipped with thicker high-performance NACA 6-series airfoils to reduce profile power. The blade also changed to a tapered planform with the maximum blade chord at the root to achieve required flap stiffness. The blade twist distribution was changed to a tri-linear distribution along the blade to find a preliminary performance compromise between hover/climb and forward flight based on flight conditions at that time provided by the Mobility team. In particular, inboard twist close to the root was kept close to constant and notably lower than in Phase A to prevent stall in expected descent conditions.

Fixed-pitch, speed-controlled rotors experience a wide range of excitation frequencies due to the large range in operating rpm. This makes placing blade structural frequencies more challenging than for variable-pitch, constant-speed rotors, particularly for two-bladed rotors such as those considered at that time. Figure 12 shows a fan plot with first flap frequencies for both the Phase B and Phase B* rotors. Note that first edgewise and torsional frequencies are not shown as they are higher than the first flap frequency of the metal rotors.

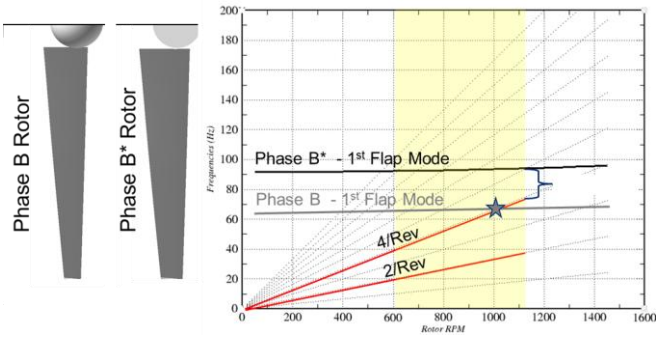


Figure 12. Phase B vs Phase B* - Placement of 1st blade flap frequency versus rotor speed.

Due to upper/lower rotor interaction of the two-bladed coaxial rotor system, placing the first blade flap natural frequency above the highest (i.e. highest rpm) strong two-bladed 4/rev excitation was considered as a requirement based on RCAS analyses to ensure that the rotors can operate at any rotational speed without adverse resonance effects. This is different from conventional Earth-based rotorcraft with flexible blades operating at constant rotor speed; here a rotor during startup or shutdown typically moves through the first blade flap frequency without adverse vibrations. This is unfortunately not the case for *Dragonfly* in its multi-rotor configuration where each rotor operates at any speed between approx. 100 rpm and a maximum rpm of around 1150, with the yellow-shaded region in Figure 12 showing the most typical range of all eight rotors. As the structural layout of the Phase B rotor matured, it became evident that the first blade flap natural frequency was lower than required, indicated by the star symbol in Figure 12. In fact, the first blade flap frequency of a manufacturable Phase B rotor would cross the strong 4/rev excitation from the two-bladed rotor system at a very typical high rotor speed. Consequently, the preliminary Phase B rotor design did not close because of structural requirements for flight at Titan.

Dragonfly Phase B* (2021-2022)

Lessons learned from this design iteration prompted the Phase B* rotor design. Similar in tapered planform, the Phase B* rotor had increased solidity compared to the Phase B rotor, see Figure 4, thereby also having lower rotor speed and a resultant lower max. 4/rev by design (not directly shown in

Figure 12). The increased solidity not only increased figure of merit but indeed brought the first blade flap natural frequency above the highest 4/rev, see Figure 12. This was due to, in part, a larger root chord. This also made the metal rotor blades lighter due to parallel developments in the rotor manufacturing process towards hollow metal blades where blade halves are fused by electron beam welding, see later section. In fact, a resulting thinner skin thickness was able to carry the dynamic loads with higher area moment of inertia because of higher absolute thickness of blade sections.

Concurrently, preliminary studies were performed concerning robustness of the design to anticipated changes in blade surface roughness through operation in the Titan environment. In addition, the likelihood of blade surface and tip vortex condensation that may obscure camera view became an important consideration for airfoil choice. Reference 33 provides a focused analysis on the subject using blade-resolved CFD analyses using StarCCM+. Lastly, consistent blade performance across a broad Reynolds-number range was a major consideration for the choice of blade airfoils. At the time, plans for testing full-scale flight-like equipment in the NASA Langley Transonic Dynamics Tunnel (TDT) in heavy gas and air at ambient temperature matured. The TDT enables testing flight-like hardware at accurate full-scale dynamic loads by testing in a medium of similar density and exact Mach number compared to Titan. However, testing in the TDT occurs at 1/6th – 1/3rd Reynolds number compared to Titan conditions, see Ref. 22. This was one of the most important considerations when choosing the airfoil series as the anticipated TDT tests would be the only opportunity to quantify model prediction uncertainty to be used by the Mobility team in closed-loop simulations of a *Dragonfly* digital twin. A summary of airfoil criteria is shown in Figure 13. As a result of these studies, the airfoil series was changed to the NACA 44-series based on its fortuitous Reynolds scaling behavior, available surface roughness data (Ref. 34), and low suction peak to suppress surface and tip vortex condensation.

Dragonfly Airfoil Table		Re Low	Re High	Mach Low	Mach High	Importance
$c_{l\,max}$	1.2 - 1.4	500,000	3 x 10^6	0	0.4	Medium
$c_{l\,min}$	-0.8	500,000	3 x 10^6	0	0.4	Medium
$c_{d\,min}$	0.01 - 0.02	500,000	3 x 10^6	0	0.4	Low
c_m	-0.05< x < -0.15	500,000	3 x 10^6	0	0.4	Low
Thickness Ratio t/c	9% - 24 %					Medium
Stall Behavior	Docile					High
Roughness Tolerance Minimize Condensation Manufacturability	Minimize Impact					High
Reynolds Scaling	Reliable data available for large AOA range Family of airfoils for different radial t/c ratios.					High

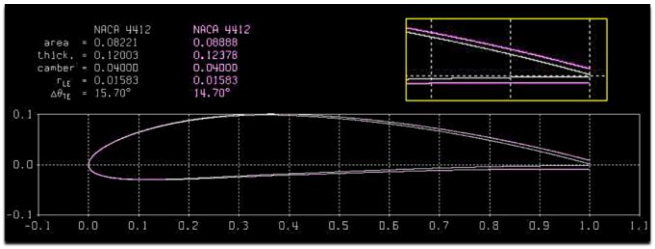


Figure 13. Phase B* airfoil criteria and series.

The airfoil series also has a benign stall behavior with a predominant smooth trailing-edge stall where the lift coefficient does not drop off rapidly beyond its maximum value, see Figure 6 for the inboard stations. In particular, the blunt trailing edge and large trailing-edge angle (no reflex camber) were advantageous for the manufacturing process and to carry normal and shear stresses during dynamic loading. In this context, combined manufacturing and stress analyses resulted in a requirement of a nearly constant 0.030 inches trailing-edge thickness. This could be easily achieved with the NACA 44-series airfoils by practically designing the blade with a truncated chord length such that subsequent clipping at the actual desired chord length resulted in a constant-thickness trailing edge along the entire blade. Figure 13 illustrates the original and clipped truncated airfoil close to the blade tip. CFD analyses verified that this slight modification to the airfoils practically did not alter their performance, though C81 tables were generated for the actual clipped airfoils for use in RCAS comprehensive analysis, as well as in RotCFD and STAR-CCM+ VDM simulations.

The Phase B* rotor also had a slightly modified taper ratio compared to the Phase B rotor. This was a result of parallel motor developments and the associated size of the mounting plate to attach to the blade hub. Specifically, the root chord and taper ratio were adjusted to enable a very streamlined hub design for the stiff rotors. It was indeed confirmed with high-fidelity CFD analyses that blade flow was attached to the blades up to the hub in hover and forward flight. This reduced rotor power itself and the parasite power of the rigid hub. As for the blade twist distribution, the tri-linear approach from Phase B balancing hover, climb, cruise, forward flight, and descent was more formalized by a continuous analytical distribution. In essence, the legacy twist distribution (as it was termed later), starts off with a hyperbolic distribution close to the blade tip for good hover performance, then blends into a linear mid-blade section suitable for forward flight, and ends flat in a cosine function close to the blade root, see also later sections on Phase C design and optimization.

The two-bladed coaxial Phase B* rotor became the first closed design for the *Dragonfly* lander. This rotor passed the preliminary design review (PDR) and was subsequently and successfully tested in the NASA TDT in 2022, see Ref. 22.

Dragonfly Phase C (2022-2023)

Post the Aerodynamics PDR and with further maturation of the mission flight profile provided by the Mobility group, a systematic study was sought towards optimizing the *Dragonfly* rotors by extracting any remaining and feasible small overall rotor performance improvements. Rotor performance gains would also improve vehicle range through its many anticipated flight profiles, including scouts and leapfrogs. For most of the design variants, the tapered planform was maintained due to its proven structural properties and manufacturability based on the closed Phase B* rotor design. Rotor design parameters included solidity (weight, rotor inertia), design lift coefficient (torque, climb performance, stall margin in descent), and blade twist

(compromise between hover, climb, cruise, and descent). Table 5 shows the conditions of a particular leapfrog flight profile provided by the Mobility team. These conditions were used for both the early Phase C trade study and later optimization efforts for the three-bladed configuration.

The conditions listed in Table 5 refer to average values over all eight rotors in trimmed flight. In this particular leapfrog sequence, the *Dragonfly* lander climbs out of hover to cruise altitude, traverses in cruise to a specified distance to scout out a new landing site, then flies back and descends towards a known landing site, with a net range of 4km from its starting point. The Phase C design requirements were to minimize the overall total energy required to fly the leapfrog mission, avoid stall in descent, maintain blade stiffness with concurrent structural layout, and satisfy the so-called sticky-ground requirement to provide a total of 530 N combined upper/lower rotor thrust at no more than 1050 rpm (based on analyses of adhesion strength of the *Dragonfly* lander's skids on an assumed worst-case wet Titan surface). Lastly, the Phase C design was not to exceed rotor torque at any flight condition compared to the Phase B* rotor by more than 1 Nm. This opportunity in the blade design space was approved by the motor development team.

Table 5. Dragonfly mission conditions and % segment time used for Phase C rotor design and optimization.

	RPM	AOA [◦]	V [M/S]	% TIME AT CONDITION
HOVER	854	0.0	0.0	N/A
CLIMB	978	-28.3	6.9	15.2%
CRUISE	706	-9.6	8.0	60.5%
DESCENT	604	17.7	4.5	23.3%
SCOUT	754	-3.7	4.0	1.0%

Figure 14 brings the data shown in Table 5 into a different perspective, contrasting time spent in a flight condition against actual energy use at that condition, see also Ref. 35.

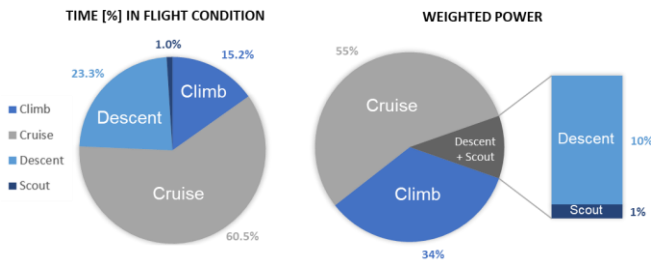


Figure 14. *Dragonfly* Leapfrog – Time vs. Energy.

Here the climb condition stands out: the *Dragonfly* lander only spends 15% of its time in climb, but climbing accounts for 34% of the energy required. The opposite trend is true for the descent condition: more time is spent in descent than in climb, but at notably reduced energy use. The pie charts in Figure 14 signify that in order to minimize energy usage over the leapfrog mission, a Phase C rotor design might be less performing in descent compared to the Phase B* rotor (albeit not stalling), but that this can likely be outweighed with improved performance in climb and forward flight. In this context, it is important to emphasize that compared to Earth-based multi-copter vehicles, *Dragonfly* has a brief cruise leg with approximately 60% of the time spent in scout or cruise. This had a profound impact on the best rotor blade design resulting from this systematic study which favored a tapered planform and the particular type of blade twist distribution described earlier. For reference, a reduction of 1% in energy use over a leapfrog mission of 0.69 hours (Total Energy: 3.809 kWh) corresponds to a net gain in range of 217m (or 5.4% of 4km net range), if all energy savings are spent in additional cruise distance.

A total of 12 design variations were considered in a trade study and analyzed using RotCFD VDM in coordination with structural analyses in RCAS. These are summarized in Table 6 along with their performance in terms of energy usage over the leapfrog mission compared to that of the Phase B* rotor.

Table 6. Design Variations - Phase B* to Phase C. (ΔEnergy [%] savings over Leapfrog flight)

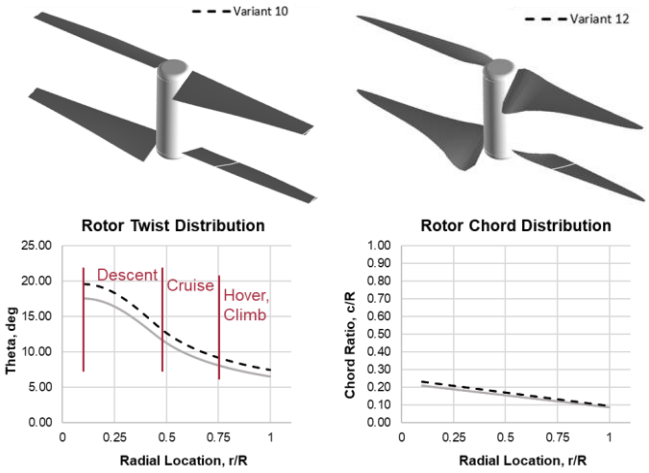
Phase B* Variant	Design Change	ΔEnergy [%]
V1	Round Tip Chord	-1.0
V2	+ Root Twist	-0.8
V3	- Root Twist	+1.8
V4	- Radial Twist	+6.8
V5	+ Tip Twist	-0.1
V6	+ Collective	-1.6
V7	- Airfoil Thickness	-1.1
V8	+ 10% σ (Phase B* taper)	-1.2
V9	+ 10% σ (7% Root, 15% Tip)	-0.6
Phase C V10	+ 10% σ (Phase B* taper) + 10% Design c_l	**-1.8**
V11	+ 10% σ (7% Root, 15% Tip) + 10% Design c_l	-1.8
V12	Free Design FM & Climb L/D_e	-0.8

In the following, brief summaries are given as to their respective performance over the leapfrog mission flight profile and the resultant convergence to the Phase C rotor (i.e. V10 in Table 6). Performance of the design variants listed in Table 6 is as follows:

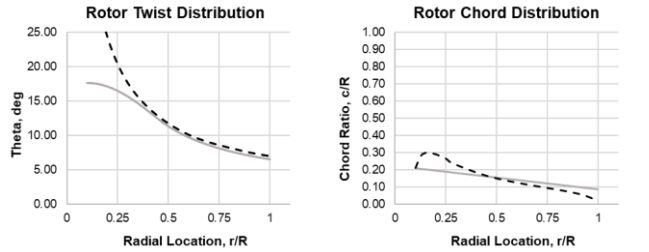
V1: Based on feedback received at the Aero PDR, a carefully designed rounded tip shape (chord going to zero) was hypothesized to have improved performance based on optimum propeller theory. Indeed, this was the case as seen in Table 6, primarily enabled by improved hover and climb performance. This rotor satisfied all requirements of a feasible

Phase C design. – V2, V3: Similar energy savings were enabled by the V2 variant rotor with approx. 5 deg more root twist. This rotor, however, resulted in insufficient stall margin in descent. In contrast, the V3 variant rotor with approx. 5 deg less root twist performed equally worse at all flight conditions. This was a result of a practically lower mean lift coefficient, resulting in higher tip speed for a required trimmed thrust and hence higher profile power. The combined V2 and V3 analysis provided a first hint that the Phase B* twist distribution was one that indeed strikes a good balance between the various conflicting flight conditions. – V4, V5, V6: These design variants essentially investigated in more detail the effect of the design (or mean) lift coefficient, with V4 lowering and V6 increasing the mean lift coefficient along the blade. The V5 variant rotor considered a gradual 2.5deg twist increase between the 75% blade station and the tip, with a small benefit in hover but only a very minor effect on energy use over the leapfrog profile. The V4 variant rotor was clearly underperforming as the essentially lower design lift coefficient required notable higher rotor speed for trimmed required thrust, see also Figure 4 for the performance dependence on mean lift coefficient. In contrast, the V6 variant rotor became of interest as a slightly higher resulting mean lift coefficient improved performance while only losing a small amount of stall margin in descent. – V7: This variant rotor explored indirectly the possibility of manufacturing the *Dragonfly* rotors out of Titanium instead of Aluminum (a program consideration at that time), enabling a reduction in airfoil thickness at the root from 24% to 21% and gradually blending into the baseline tip thickness. The reduced profile power resulted in energy savings of about 1% which was not considered substantial with respect to the increased time and cost associated with developing and manufacturing Titanium rotors. – V8: This design variant explored a small increase in rotor solidity with an associated increase in performance and satisfied all requirements. Here again, a small increase in rotor solidity essentially reduced rotor speed for a required trimmed thrust, thereby reducing profile power, see also Figure 4 for general performance metrics versus solidity. Hence this variant was considered a viable candidate. – V9, V10, V11: These design variants were based on lessons learned from V6 and V8, looking at feasible increments in mean lift coefficient and solidity and exploiting the extra available 1 Nm in rotor torque. These formed the basis for choosing the V10 variant rotor as the Phase C rotor as it satisfied all requirements. The V11 variant, though a bit higher performing than V10, was discarded because of its slightly worse descent performance. The V10 variant resulted in an overall energy savings of 1.8% compared to the baseline (V0) Phase B* rotor. – V12: This last variant was considered as a demonstration that opening the full design space of blade planform and twist distribution would likely not result in large further improvements. This rotor was obtained using an optimization procedure for axial propellers using a helicoidal vortex method (Ref. 36). While outperforming V10 in hover and climb, the V12 variant overall performed worse in comparison and stalled in descent, which disqualified it as a feasible design.

Figure 15 shows Variant 10, which became the Phase C rotor, and Variant 12 as an extreme example of planform shapes considered. The grey lines in the plots represent Phase B*.



(a) Phase C (V10) vs. Phase B*



(b) V12 vs. Phase B*

Figure 15. Rotor Design Trade Studies. Phase B*(grey lines), Phase C (V10), V12 (black lines).

This shows that the practical tapered planform shape and twist distribution described in an earlier section of the Phase B* rotor were essentially maintained. The addition of V12 to Figure 15 is simply to demonstrate that the Phase B* design was already quite mature and optimal, with drastic changes in the design not being further expected. In this context, the V1 variant rotor with a chord distribution similar to V12 in the tip region, while satisfying all requirements, was discarded due to its lower performance gains compared to V10 and concerns with Reynolds scalability between the anticipated TDT tests and Titan conditions. Specifically, it was expected that the blade tip vortex formation and separation from the surface are likely dependent on Reynolds number. A finite-chord tip with a flat end, on the other hand, has a defined edge from which the tip vortex separates from the surface. These considerations combined with concerns about manufacturability practically set the tapered planform of the Phase B* and Phase C (V10) rotors as the final planform shape for the *Dragonfly* rotors.

Figure 16 contrasts the weighted power values (Weighted Power [W] = %Time at Flight Condition, Table 5 * Power) of the Phase C and Phase B* rotors. It can be seen that power reductions in hover, climb, and cruise enable an overall

reduction in energy required per leapfrog mission completed. The 1.8% energy savings over a leapfrog correspond to a notable increase in cruise distance of 390 m (or 9.75% of 4km net range), if all energy savings are spent in cruise distance. Also note that the Phase B* rotor failed the sticky-ground requirement described earlier and did not achieve a hover thrust of 530 N at 1050 rpm by only a few Newtons.

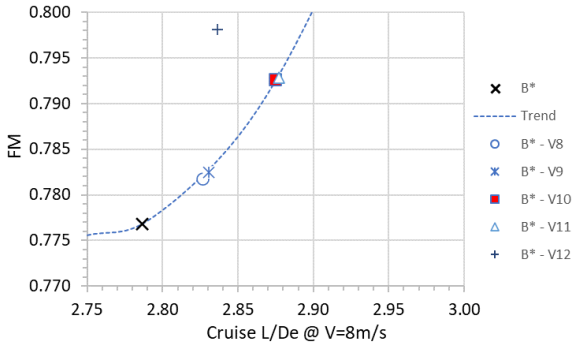


	POWER [W]	WEIGHTED POWER [W]	POWER [W]	WEIGHTED POWER [W]
STICKY GROUND	Fail	0.0	3888	0.0
CLIMB	3099	471	3023	460
CRUISE	1259	761	1234	747
DESCENT	574	134	584	136
SCOUT	1384	14	1358	14
ENERGY (LEAPFROG)	3.809 kWh		3.742 kWh (-1.8%)	

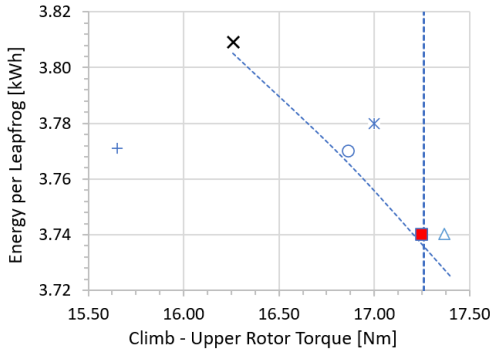
Figure 16. Rotor Design Optimization.
Energy per Leapfrog - Phase B* vs. Phase C (V10)

Figure 17 shows a compelling illustration of various rotor performance parameters contrasting the Phase B* rotor against its variants V8-V12. In Figure 17a, it can be seen that V8-V11 all have higher FM and L/D_e in cruise compared to the Phase B* baseline. In contrast, the extreme V12 variant has the highest FM but falls short of V10 (Phase C) and V11 in terms of cruise L/D_e. Figure 17b shows energy use per Leapfrog versus upper rotor torque in climb. These represent the objective function of energy use and the torque constraint (blue vertical line) described earlier (i.e. max. of 1 Nm delta torque compared to the Phase B* rotor in that condition). It can be seen that the V12 variant excels in rotor torque in climb, requiring about 1 Nm less torque compared to Phase B*; however it only achieves about half of the energy savings compared to the V10 (Phase C) and V11 design variants. A trendline is shown in Figure 17b whose slope indicates the sensitivity of reducing energy requirements with torque increases in climb. Figure 17c plots descent L/D_e versus cruise L/D_e. Note that the L/D_e in descent is about twice as high as in cruise due to the significantly less rotor power required in trimmed descent. Also here, a clear trend can be seen that descent L/D_e actually decreases, but climb L/De increases from Phase B* through variants V9-V11. This clearly demonstrates the tradeoff in *Dragonfly* rotor performance between the various conflicting flight conditions. Once more it is apparent that while the V12 variant rotor has the highest climb L/D_e, it significantly loses in descent L/D_e, leading ultimately to less optimal performance over the leapfrog mission.

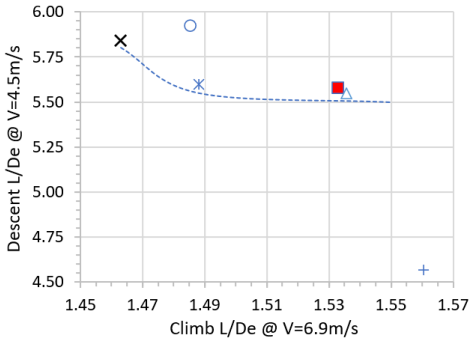
The V10 variant rotor moved forward as the two-bladed Phase C rotor. In addition to the leapfrog mission, this rotor was also shown to result in similar gains during first flight, during which the *Dragonfly* lander scouts out its first landing site and descends down to the surface and during an atmospheric profiling campaign which essentially consists solely of climb and descent. At this stage in the program, it was understood that the preliminary rotor design efforts had matured sufficiently to advance to the detailed design stage.



(a) FM versus Cruise L/D_e.



(b) Energy per leapfrog versus rotor torque in climb.



(c) Descent L/De versus Climb L/D_e.

Figure 17. Rotor Design Trade Studies.
Phase B*(black cross), Phase C (V10, red square)

Concurrent increases in *Dragonfly* vehicle mass during Phase B, structural design and tailoring of rotor sting arms within a tighter mass balance, and detailed modeling of vibratory levels at scientific instruments inside the lander made it increasingly challenging to handle the vibrations of the two-bladed rotor system that had grown according with vehicle mass since Phase A. Among other design and damping considerations on the lander body, this prompted consideration of a feasible three-bladed variant of the chosen Phase C rotor with practically similar performance. As

indicated by the red line on the Phase C planform in Figure 16 (and Figure 2), both rotor disk area and rotor solidity were maintained, with the three-bladed variant having 2/3rd of the chord for each blade compared to the two-bladed Phase C baseline rotor. The Phase C twist distribution was also maintained. From a rotor performance perspective, it was verified using RotCFD and STAR-CCM+ VDM (see later section) that Phase C rotor performance of the two-bladed and three-bladed variants were practically the same. In this context, it is interesting to note that the three-bladed rotor operates at 2/3rd sectional Reynolds number (basically $2x10^6$ versus $3x10^6$ in Table 1) compared to the two-bladed baseline Phase C rotor. The small increase in profile power was practically negated by reduced tip loss of the three-bladed versus the two-bladed rotor system. Both two-bladed and three-bladed Phase C rotors moved forward to the detailed design process outlined in the next section.

DETAILED DESIGN

Dragonfly Phase C (2023-2025)

The same computational tool set of RotCFD and STAR-CCM+ VDM as well as RCAS was still applied in early Phase C when instrument placement within the *Dragonfly* lander body and increased vehicle mass resulted in ultimately unfavorable vibration levels for scientific instruments. Rotor loads and vibrations were simulated in RCAS coupled with the Viscous Vortex Particle Method (VVPM) inflow model. An elastic fuselage modal model, generated by the NASTRAN FEA, was used to represent the dynamics of the *Dragonfly* lander in the simulations. Simulations of the hub loads and lander vibrations were conducted at multiple flight conditions for both two- and three-bladed Phase C rotor configurations. Figure 18 shows a high-level overview of the aeroelastic modeling and analysis.

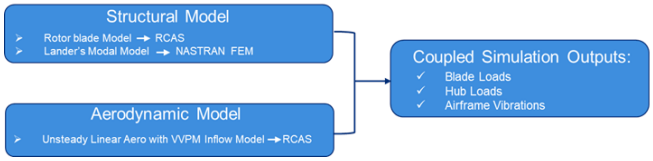


Figure 18. Overview of Aeroelastic Modeling.

Figure 19 shows the comparison of the N/rev vibrations at two of the critical instrument locations, namely the light detection and ranging (LiDAR) sensor and the Miniature Inertial Measurement Unit (MIMU) at the cruise flight condition. The cumulative root sum square (RSS) vibration levels are significantly smaller for a three-bladed rotor. Similar levels of reduction were noted at climb, descent, and scout conditions.

For a two-bladed rotor in general, inertia is periodic in the following sense: the inertia of the rotor about any horizontal axis in the fixed/earth frame varies as a function of rotor position. The inertia is maximum when the blades are perpendicular to this axis, and minimum when parallel. This quality is unique to two blade rotors. Because of the periodic inertia, an input at 2/rev frequency produces a response at all even harmonics of the spin rate. This is referred to as the "cascading effect" and is the primary cause of significant vibration issues in a two-bladed rotor. This is also the reason why in Figure 12 the first blade flap frequency has to be set higher than the highest 4/rev excitation, simply because 4/rev vibrations are high for a two-bladed system.

More blades, on the other hand, result in less vibrations for two reasons. First, the mathematics of a rotor with N blades is such that the loads from individual blades sum to partially cancel at the rotor hub leaving only N/rev and its multiples to filter into the fuselage. Hence, more blades lead to more of these loads being canceled out. Second, airload harmonics drop off in magnitude at higher harmonics, so N/rev airloads when N is large are smaller than when N is less. Therefore, the three-bladed rotor produces significantly less vibrations than the two-bladed design. This also means that the 6/rev harmonic amplification for the three-bladed rotor was much smaller than the 4/rev for the two-bladed design. With reference to Figure 12, a three-bladed rotor at lower chord has a bit lower first blade flap frequency compared to the two-bladed design (because it has 2/3rd chord at the same total rotor solidity); however, the flap frequency has to remain only higher than 3/rev as the 6/rev harmonic is quite low and does not present resonance challenges. Hence a three-bladed Phase C rotor is indeed both aerodynamically and structurally feasible for the *Dragonfly* lander.

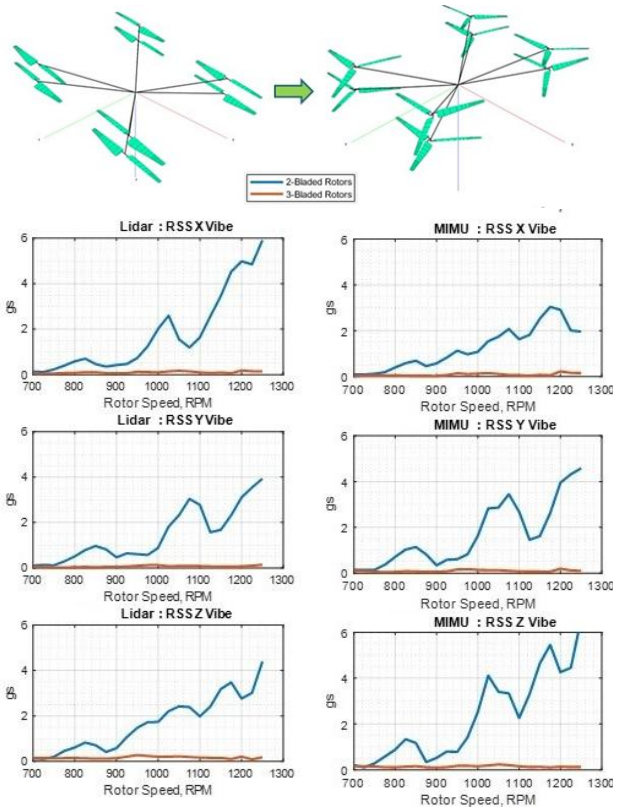


Figure 19. Accelerations at LiDAR and MIMU for a two-bladed vs. a three-bladed Phase C.

Ultimately, based on projected cost and mechanical complexity of alternative means to reduce instrument vibratory levels (including rotor arm braces, dampening material/devices, etc.) and analyses including weight penalties, the design transitioned to the three-bladed rotor system of the same disk area but reduced fore-aft rotor separation distance. The fore-aft reduction was required due to the fixed-diameter packaging constraint of the backshell. This resulted in an associated penalty on power required in cruise, as vehicle pitch attitude is more difficult to control and resulted in lowering the actual cruise speed. In the end, though, the new blade design, i.e. the three-bladed Phase C rotor, was simple and maintained rotor solidity and mean lift coefficient (with all their proven performance properties), albeit with a small weight penalty. As mentioned in a previous section, the three-bladed Phase C rotor has a reduced blade chord by 2/3rd compared to the original two-bladed Phase C rotor (see the red line in Figure 2 and 16).

Discrete blade CFD was conducted in STAR-CCM+ to assess the aerodynamic performance impacts of the transition from a two-bladed to a three-bladed rotor. A single rotor in hover was assessed at 900 RPM. Results for both the two-bladed and three-bladed designs are shown in Figure 20, showing highly comparable results between the two rotors. Thrust for the two designs is essentially equivalent, while the three-bladed design has slightly lower torque and slightly higher FM than the two-bladed design. Figure 21 shows a visualization of this case for the three-bladed design.

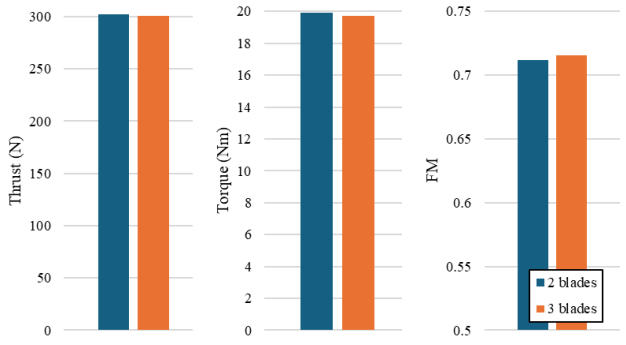


Figure 20. STAR-CCM+ Discrete Blade Isolated Rotor. (Hover Results for 2- vs. 3-bladed Rotor Designs)

An isolated coaxial pair was assessed in a nominal cruise condition at 8 m/s, with a shaft angle of -9.6 degrees, at 706 RPM. Results for both the two-bladed and three-bladed designs are shown in Figure 22, again showing comparable results between the two designs. For both the upper and lower rotors, the three-bladed design has slightly higher thrust and slightly lower torque than the two-bladed design. Additionally, the overall rotor pair efficiency is slightly higher for the three-bladed design than for the two-bladed design. Figure 23 shows a visualization of this cruise case for the three-bladed design.



Figure 21. STAR-CCM+ Discrete Blade Solution in Hover Showing Iso-Vorticity Contours.

Planform Optimization Study (2024)

After the transition from a two- to a three-bladed design, an additional optimization study was undertaken to assess available performance improvements with change to the blade planform and twist distribution, Ref. 37. It was shown that small performance improvements were theoretically possible at certain conditions, though not all hard constraints of the evolved rotor planform were accounted for in the investigation. The program then decided to keep the proven blade planform as is. A further study was then limited to a twist optimization of the three-bladed Phase C planform. The airfoil distribution was similarly maintained, with a slight adjustment to the trailing-edge profile of the airfoils to maintain a 0.030 inches thickness for manufacturing constraints.

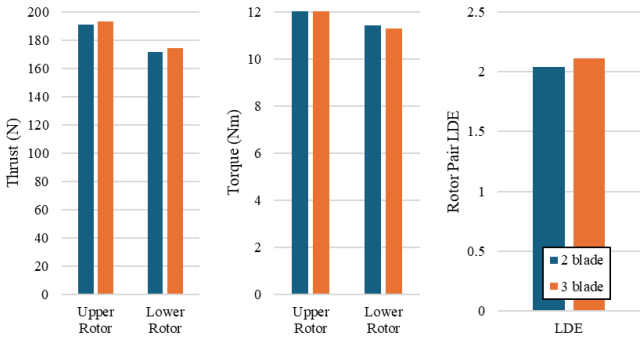


Figure 22. STAR-CCM+ Discrete Blade Isolated Coax. (Cruise Results for 2 vs. 3 bladed Rotor Designs)

Two parallel approaches were taken for the study: a Sikorsky Maryland Free Wake Genetic Algorithm (SAC-MFW-GA) and a coupled Simcenter STAR-CCM+/HEEDS (Hierarchical Efficient Evolutionary Design Synthesis).

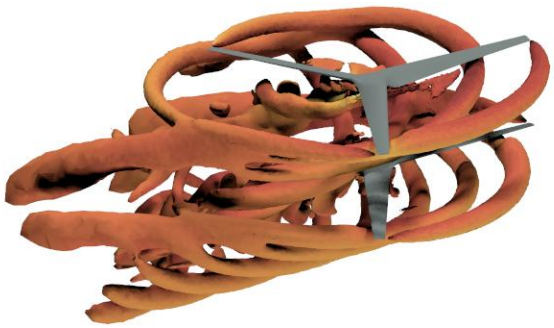


Figure 23. STAR-CCM+ Discrete Blade Solution in Forward Flight Showing Iso-Vorticity Contours.

The SAC-MFW-GA approach is a Weissinger-L lifting surface model for blade aerodynamics calculated using C81 tables combined with full-span distorted free-wake modeling, wrapped in a genetic algorithm optimization that balances hover and cruise performance metrics. This fast-running solver was able to assess 40 chromosomes for 30 generations, yielding a total of 1200 potential designs. In this approach, a two-part optimization was conducted, with equal weighting on FM in hover and L/D_e in cruise. Figure 24 shows the pareto front of these metrics across the different generations of the optimization as compared with the baseline design.

The STAR-CCM+/HEEDS approach leveraged the Virtual Disk Model (VDM) approach which is being used to generate the aerodynamic databases feeding the Dragonfly lander Mobility flight model, see Refs. 14, 23, 25. The VDM implementation is discussed in the above Design Tools section. The design space exploration and optimization package Simcenter HEEDS was used to automate execution of virtual disk simulations in hover and four forward flight conditions in a standard flight as the twist profile was varied, with the goal of maximizing hover figure of merit (FM) while minimizing required power weighted over time spent in the four forward flight conditions listed in Table 5.

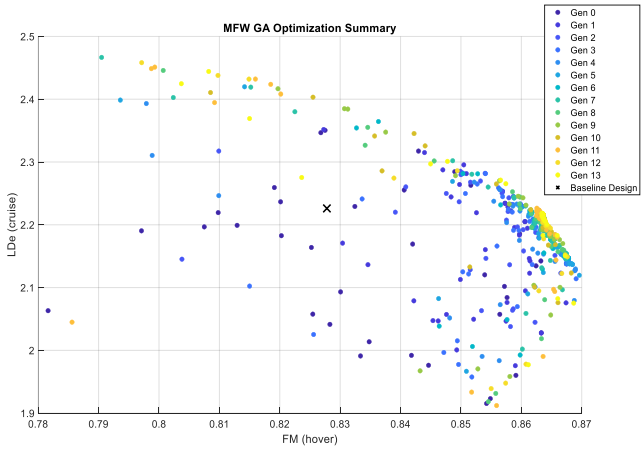


Figure 24. Phase C three-bladed MFW Optimization Pareto front using a genetic algorithm.

A MATLAB script was utilized to generate a new twist distribution for each case, which was constrained to be within +/-5 degrees of the nominal twist. The twist values at 4 control points at fixed radial stations at the root, 0.50R, 0.75R, and tip were independently varied, and a smoothed twist distribution was generated from these points, see Figure 25. This twist distribution was then read into the Virtual Disk definitions for the STAR-CCM+ runs for each case. A total of 100 designs were executed. Twist distributions and results for the top 4 designs along the pareto front are shown in Figure 26.

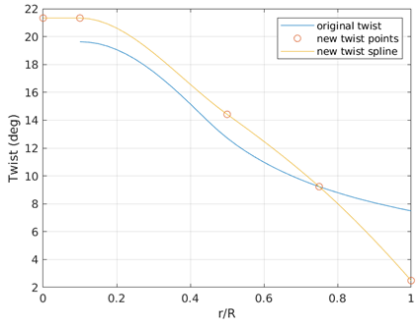


Figure 25. HEEDS - Sample Twist Distribution.

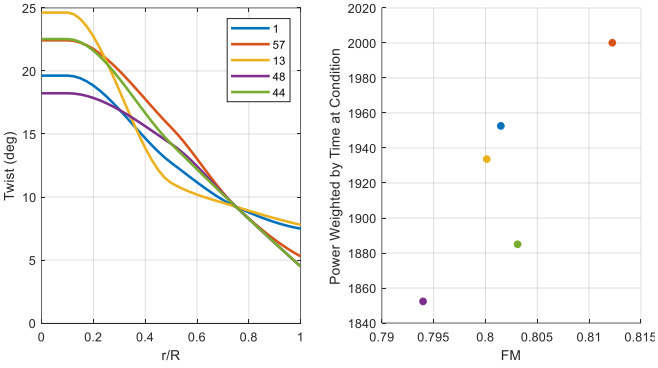


Figure 26. HEEDS & STAR-CCM+ twist optimization and resulting power and FM compared to the baseline Phase C rotor (Design 1, blue).

Ultimately, both approaches of adjusting the twist distribution showed no large gains over the flight envelope, and while small improvements were available it was recommended to keep the legacy twist distribution and the accompanying confidence of a robustly tested and analyzed design. Implicitly, the vetting of the design through test and multiple numerical methods provides increased design confidence for *Dragonfly*.

Final Canted Rotor Layout (2024-2025)

The rotor configuration was reoriented from parallel coaxial rotors to oppositely canted rotor pairs. This change was driven by yaw control limitations by the Mobility team in both the forward flight and preparation for powered flight (PPF) phases of the lander mission. The overall lander flight control was assessed using the STAR-CCM+ Virtual Disk methodology to generate an aerodynamic database for use in

the Mobility closed loop flight dynamics simulation, Refs. 27-28.

Additionally, detailed high-fidelity time-accurate discrete blade simulations using both STAR-CCM+ and CREATE-AV Helios, which leveraged a structured OVERFLOW solver for the blades, were used to assess performance impacts of the move from two to three blades and parallel to oppositely canted configurations. This higher-fidelity analysis was used to verify that these changes to the rotor pair layout, while not aerodynamically driven, did not negatively impact system performance. Particularly, the goal was to assess the risk in moving from parallel rotors to an oppositely canted layout. Here the concern revolved around the rotor-to-rotor interference, as the opposing cant angle brings the outboard blade tips into closer proximity.

An isolated three-bladed rotor pair was assessed in hover for both the parallel rotor configuration and the oppositely canted rotor configuration at 900 and 1100 rpm, see Figure 27. The azimuthal orientation was set so that the blade passage of the upper and lower rotors would occur at the closest vertical separation. In flight, the rotors are rpm controlled, so the blade passage point varies, but this gave a worst-case comparison snapshot for the interference. Thrust and torque values for the upper and lower rotors are shown in Figure 27.

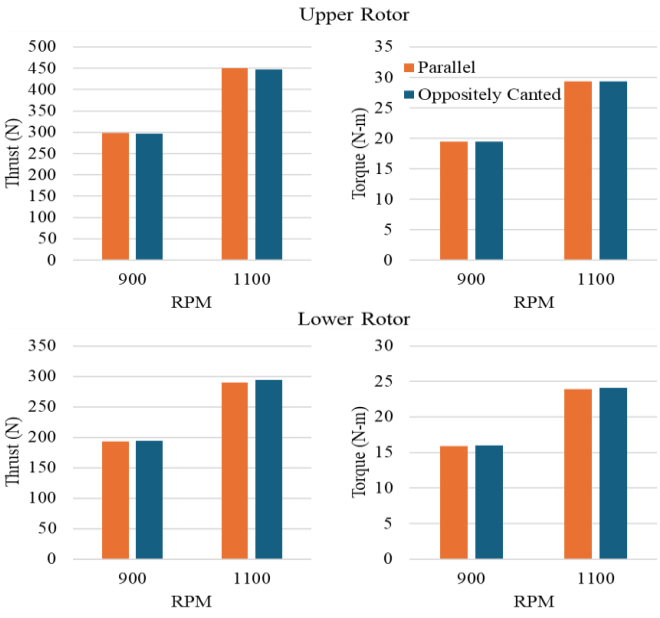


Figure 27. Loads for isolated parallel and oppositely canted rotor pairs in hover at 900 & 1100 rpm.

Differences are about 1% between configurations, with actually a small increase in FM for the canted rotor. Therefore, the change in rotor orientation has minimal impact on the aerodynamic effectiveness of the rotors. Blade elasticity was also investigated with Helios-RCAS coupling and also showed minimal vibration change associated with the reduced tip clearance.

ROTOR MANUFACTURING PROCESS

Both the two-bladed and three-bladed rotors were fabricated from Aluminum 2219-T851. This alloy was selected due to its superior material properties at cryogenic temperatures. The Dragonfly rotor design is driven by fatigue and stiffness requirements, and the alloy's Young's modulus and fatigue endurance limits increase at the expected Titan operating temperatures. The raw material is procured as plate billets, with blanks cut out on a waterjet for the rotor bases, hub closeout caps, and blade skin covers, see Figure 28a. The rotor base blank is cut to be slightly larger than the 1.35m diameter of the final rotor, so as to incorporate the hub and blades in a single piece of metal from the start. Fabrication is done such that the weld joint is always located on the suction surface of each blade, see Figure 28b. This was done in order to place that joint on the compression surface of each blade and mitigate any potential crack growth from extended tension-tension fatigue loading in forward flight.

Figure 28a shows that rough machining on the rotor bases and blade covers is conducted on a large three-axis mill to prepare both parts for electron beam welding. At this point, only the inner mold lines of the blades are machined to their final geometry, all other dimensions are left oversized. A small lip is machined into the blade cavities that allows for the blade covers to be positioned for welding. At each rotor tip, a vent hole is drilled into each blade cavity to facilitate the electron beam welding operation that is conducted at vacuum. Four blind holes are additionally drilled and tapped in front of and behind this vent hole, see Figure 28c. These are later used as balance provisions in the finished rotors.

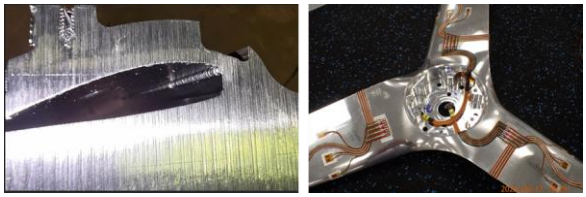
The rotor bases and covers are then prepared for welding by precision cleaning, and fit checks are conducted to ensure gaps are allowable between the two pieces. The cover is clamped in place, and tack welds are laid down in the initial vacuum and welding cycle. Once the tack welds are in place, the clamp between the covers and the base is removed, and the full perimeter penetration weld is performed. The final weld leaves an internal fillet between the base and the cover, fully fusing the two components together, see Figure 28b. For this particular operation, weld schedule development and welding services from Precision Technologies in Enfield, CT, were employed.

Once welding is completed, the welded rotor assembly is heat treated to artificially age material in the weld heat-affected zone. After this heat treatment, the rotor is placed back into the three-axis mill for final machining. The suction surface of each blade is machined to the final geometry first, see Figure 28c. The rotor is then rotated and placed on a vacuum tooling fixture that fully supports the span of the rotor, and the pressure surface of each blade is finished as well as the trailing edges. The trailing edges are truncated to allow for machineability and are finished to approximately 0.030 inches thickness. The outer third of each rotor is polished to a surface finish better than 32 microinches in order to meet

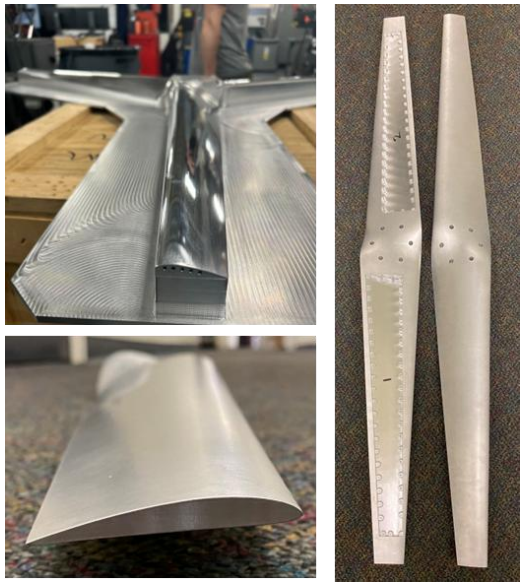
aerodynamic roughness requirements. The finished rotors are then inspected, and the external surfaces are conversion coated. Due to the asymmetric nature of the welding, a small amount of warping is induced that was considered as a small pre-cone angle with little aerodynamic effect, see Ref. 22.



(a) Rough machining (Left: Phase B*, 2-bladed; Right: Phase C, 3-bladed)



(b) Machining & Instrumentation (Phase C, 3-bladed)
(Left: Electron beam weld, Right: Strain gauge installation)



(c) Final machining (Phase B*, 2-bladed; Phase C, 3-bladed)

Figure 28. Rotor Manufacturing Process, 2022-2025. (Phase B*, 2-bladed; Phase C, 3-bladed)
Final *Dragonfly* Rotor = Phase C, 3-bladed

Figure 28c also shows the final two-bladed Phase B* rotor that was tested in the TDT-1 entry. For the three-bladed rotors that were subsequently tested in the TDT-2A test entry, strain gauges were installed at three spanwise locations on each blade and checked out through static loading, see Figure 28b. The rotors were subsequently statically balanced by installing tungsten and steel set screws at necessary blade tips while the rotor was suspended through its spin axis. Dynamic balance checks were also performed. Finally, a rap test was conducted in both the free-free and fixed conditions to verify the rotor's modal behavior as compared to analytical predictions.

The *Dragonfly* mission has manufactured several sets of full-scale rotors for wind tunnel and fatigue testing, leading to the upcoming build of the flight rotor set that will launch to Titan. There are four unique rotor geometries as seen in Figure 1c, i.e. upper clockwise, upper counter-clockwise, lower clockwise, and lower counter-clockwise. The flight vehicle will incorporate two of each geometry in the final assembly. Each rotor is of a monolithic design with fixed-pitch blades. There is no joint between the hub and blades, nor are there any flap, pitch, or lead-lag hinges. The blades themselves are hollow in order to optimize mass and inertia, with skins approximately 2mm in thickness outboard of the 1/3 span location. Thicker skins and a stiffening feature are employed in the inner third of each rotor blade inner mold line in order to tune the first flap frequency of the rotor and to reinforce highly-loaded areas.

The production methods for the flight rotors closely mirror the methods and geometry of those test rotors with one key exception. The rotors that were fabricated for both the room-temperature TDT-1 and TDT-2A test entries were designed to have the correct aerodynamic geometry at room temperature, whereas the flight rotors will be machined to slightly oversized dimensions such that they contract to the prescribed aerodynamic geometry at Titan's cryogenic surface temperature. Consequently, the rotor sets tested in the wind tunnels were evaluated with reduced room-temperature material properties and expanded test matrices, conditions that were found to be more stressing than the predicted Titan flight loads and fatigue life environments.

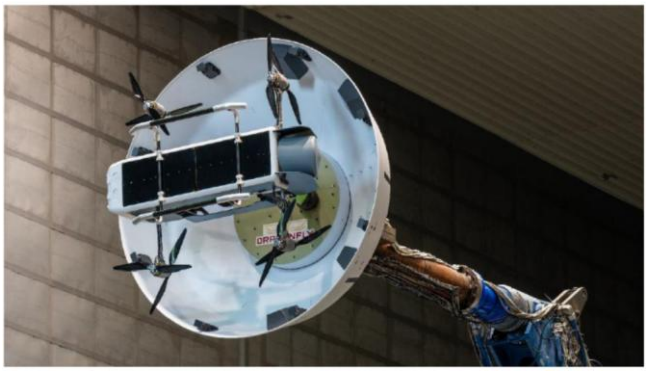
EXPERIMENTAL VALIDATION

Experimental validation efforts for *Dragonfly* rotor aerodynamics and aeromechanics have been conducted via a series of wind tunnel entries. Several focused on rotor and body interactional aerodynamics, using commercial off-the-shelf (COTS) composite rotor blades and preliminary lander models. Figure 29 shows the respective wind tunnel tests in the NASA Langley 14 ft by 22 ft subsonic wind tunnel and the National Full-Scale Aerodynamics Complex (NFAC) at the NASA Ames Research Center. They served as precursor tests for subsequent test campaigns with actual *Dragonfly* rotors and post-CDR lander configuration in the NASA Langley Transonic Dynamics Tunnel (TDT), as described further below. The tests shown in Figure 29 were important for early computational tool validation (Ref. 38) and quantifying uncertainty when testing at low wind-tunnel speed (Ref. 39). The NFAC test (Ref. 40) in particular was very valuable in identifying some critical aspects with respect to experimental and computational uncertainty (Ref. 41) and identifying rotor-body interactions causing adverse effects for yaw control authority (Refs. 7, 42-45). Ultimately, the challenges associated with yaw control identified in the

NFAC test resulted in changing the Phase C rotor design to the canted configuration seen in Figure 1c.



(a) COTS rotor and lander testing in NASA Langley 14 ft x 22 ft tunnel.
Left: Coaxial rotor pair (2020) , Right: Lander model with rotors (2022)



(b) Lander and backshell models with COTS rotors.
NFAC 40 ft x 80 ft test section (2023-2024)

Figure 29. Subscale Wind Tunnel Entries using COTS blades and preliminary lander (2020-2024).

As mentioned earlier, test campaigns of actual *Dragonfly* rotors and post-CDR lander models were conducted in a series of three tests in the NASA Langley TDT. These tests were used to quantify validation uncertainty of rotor performance and lander body loads and are described next:

Dragonfly Testing in NASA Langley TDT (2022-2026)

The TDT is a closed-circuit, continuous-flow wind tunnel with variable pressure capability which can operate at speeds between near zero and Mach 1.2, using either air or Tetrafluoroethane (R-134a) as the test medium. Because R-134a has a density greater than that of air, a 3.5-times higher Reynolds numbers can be achieved in a one atmosphere ambient temperature environment. The TDT performs aeroelastic research for fixed-wing, launch vehicle, and rotorcraft configurations, Refs. 46-47. It is a well characterized facility with a long history of aerodynamics testing and CFD validation.

Because use of R-134a in the TDT can provide Reynolds numbers of 1/3rd to half of Titan conditions at equivalent Mach numbers, velocity ratios, and dynamic pressures, *Dragonfly* has leveraged the TDT for three campaigns. The first, 'TDT-1' in 2022, shown in Figure 30, was used to provide a comprehensive dataset for the Phase B* rotor to verify rotor thrust and torque across a test matrix representing all phases of *Dragonfly*'s flight.

The *Dragonfly* team returned to the TDT in 2025 and 2026 for two tests: TDT-2A, a half-span model with 2 flight-representative rotor pairs of the CDR Phase C three-bladed, stacked, canted rotor pair design, and TDT-2B, a 68%-scaled, full vehicle model using eight commercial KDE rotors similar to those tested in Refs. 5 and 38. The TDT-2A and -2B models are shown installed in Figure 31 and Figure 32, respectively.



Figure 30. TDT-1: Coaxial Phase B* Rotor Pair (2022).

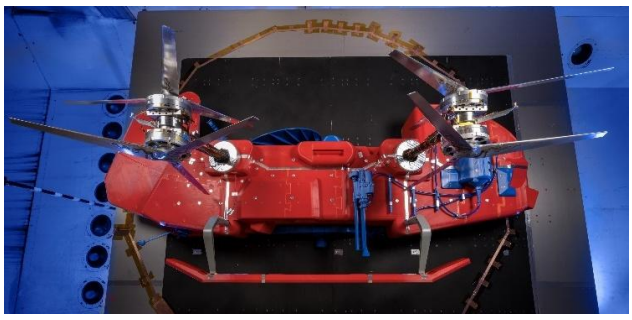


Figure 31. TDT-2A: Full-Scale Phase C Rotor Pairs with half -body *Dragonfly* lander (2025).

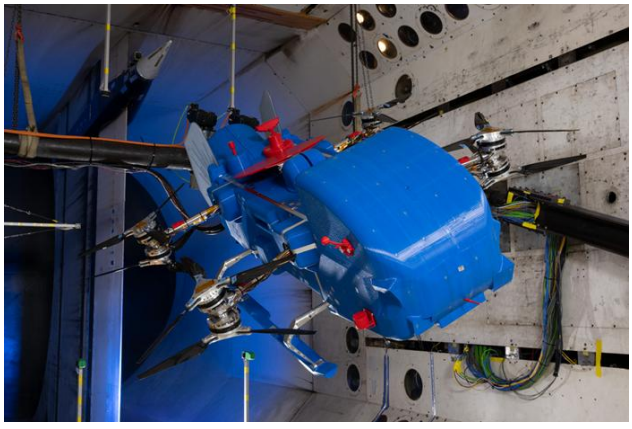


Figure 32. TDT-2B: 68%-scale lander with 4 COTS rotor pairs, capable of pitch and roll motions (2026).

TDT-1 Test Entry and Comparison to Analysis (2022)

The counter-rotating coaxial rotor was representative of the full-scale Phase B* rotors. The rotors were driven by two semi-custom KDE motors attached to ATI Omega 160 load cells mounted to a test head and elliptical strut assembly. This rotor support arm was mounted through the tunnel sidewall to the TDT Electronic Turntable. A side view of the installed rotor is provided in Figure 33, with the force and moment axes identified. The primary coaxial runs commanded both motors to the same speeds, in a nominal sequence of 430, 600, 750, 900 and/or 1100 RPM, and then back to 430 RPM. The rotor data were acquired using a Penn State system, and the wind tunnel condition data using a TDT system. Both sets of data were combined and processed by Johns Hopkins University Applied Physics Laboratory. The initial comparisons of test to analysis were performed by Penn State using the RotCFD hybrid BEMT-URANS methodology. Reference 22 provides a detailed description of the TDT-1 test entry and computational analyses.

In Figure 34a, example measured TDT data are plotted in blue, with error bars both for C_T and C_Q; computed RotCFD results are plotted in red (TDT) and black (Titan). The comparisons are conducted for 600 and 900 rpm corresponding to an average rotor speed in descent and scout/cruise. The right plot of C_T vs. μ_x is quite informative as it shows the range in C_T between axial climb and descent. The higher rpm provides the inner polar curve of lower C_T range and lowest max μ_x. The left plot of C_Q vs. C_T shows that all tunnel speeds collapse on the left branch while the right branches differentiate based on the shaft angle at which the rotor system enters VRS. In this context, note that RotCFD Titan results are computed at full-scale Reynolds number which is 3-times higher than in TDT-HG (HG = Heavy Gas) conditions.

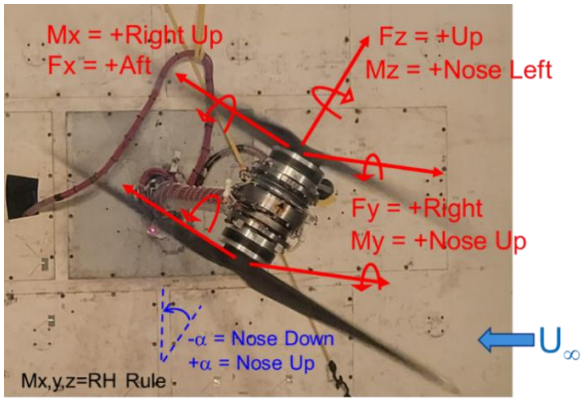
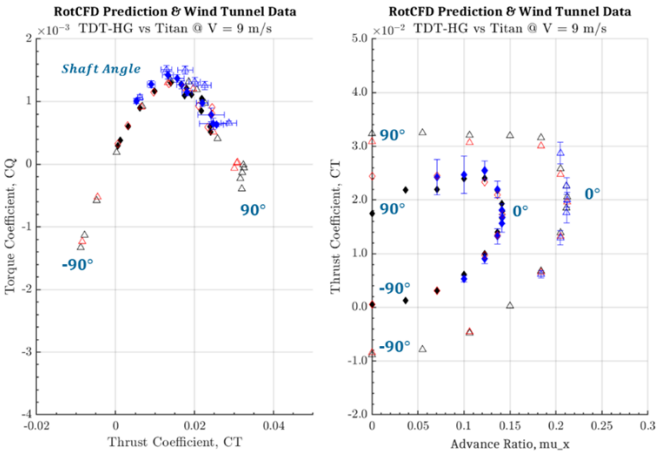
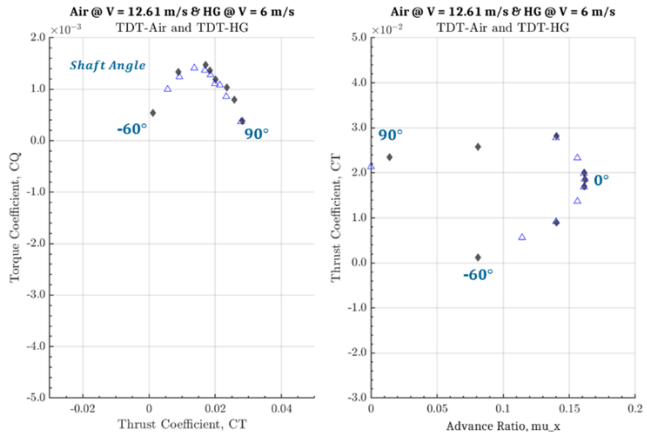


Figure 33. TDT-1 coaxial rotor side view showing coordinate axes and definition of forces and moments.

Figure 34b shows a sample Reynolds scaling experiment that was conducted in the TDT by measuring at Mach scaled conditions both in R-134a (HG) and in air. Note here that going to air as a medium resulted in an additional drop in Reynolds number by one half. The Phase B* rotor equipped with airfoils described in an earlier section does indeed give practically perfect matching in C_T, with small differences in C_Q due to increased profile power at reduced Reynolds number. In fact, Figure 34b gave confidence that a three-bladed Phase C rotor equipped with the same airfoils would indeed preserve Reynolds scaling between TDT tests and Titan conditions as the air runs in Figure 34b correspond closely to sectional Reynolds numbers of a three-bladed Phase C rotor to be tested in R-134a in a subsequent TDT-2A test.



(a) RotCFD (TDT-HG, red; Titan, black) vs. Exp. (blue). Full SA range, CRUISE speed, V = 9.0m/s.



(b) Exp. Data – TDT-Air vs TDT-HG (Mach scaled, 2x Re in TDT-HG). Full SA range, CRUISE speed, V = 9.0m/s.

Figure 34. TDT-1 - RotCFD comparison for rotor thrust and torque Reynolds scaling, from Ref. 22.

The TDT-1 test was instrumental in establishing the RotCFD Virtual Disk Method, and henceforth the STAR-CCM+ Virtual Disk Method, as the primary rotor performance analysis tool to build rotor performance tables due to its affordable computational cost to conduct hundreds of simulations and, most of all, very good predictive capability,

see Ref. 22. In addition, it confirmed that the Phase B* rotor design was robust over a wide range of Reynolds numbers. Indeed, discrepancies between RotCFD predictions in the TDT (red) and at Titan (black) are visibly smaller in Figure 34a than the differences between RotCFD results and measured data, which were mostly between 5-10%.

The TDT-1 isolated coaxial rotor data was later compared to additional analytical tools, as shown in Figure 35 for the combined rotor thrust and torque coefficients at V=9 m/s, 750 RPM, and ±60° shaft pitch. The methods include SAC-MFW, RotCFD, Helios, STAR-CCM+, and RCAS-VVPM. There is broad qualitative agreement, particularly for ±30° pitch, but some tools do better for C_T (STAR-CCM+) and some for C_Q (RotCFD). The lifting-line models, SAC-MFW and RCAS-VVPM, seem to overpredict C_T at higher pitch. Helios generally does quite well.

TDT-2A Test Setup and Example Measured Data (2025)

The TDT-2A model consisted of a half-lander model mounted on a ±90° pitch mechanism offset from a spitter plate on the east wall of the 16'x16' TDT test section. The interior non-metric structure supported the two rotor arms, and through a six-component load cell, the lander body skin. The additively manufactured skin panels were instrumented with 222 static pressure taps and 18 high-frequency response Kulite pressure transducers. Each of the 4 rotors was mounted on independent six-component load cells. Two blades of each rotor had active strain gauge flatwise and edgewise bending bridges. Additional instrumentation included 24 triaxial accelerometers and 6 Aeroprobe Corporation 15-hole Omniprobe ±150° flow angle probes around the model. Figure 36 shows additional images of the lander and the rotors.

The test plan included the full ±90° pitch range at a wide variety of freestream velocities, V, between 2.5 and 9.0 m/s. For aerodynamic performance and blade loads, the rotors were operated in pre-programmed steps between 200 and 1200 rpm, with either all rotors at the same rpm or stepped ± in pairs to provide pitch and yaw control moments. Over 2500 individual conditions were acquired.

Figure 37 shows an example of the time-averaged surface pressures on the lander at V~6 m/s, 0° pitch, and all rotors at 1025 rpm. There is yellow positive pressure on the nose and blue suction along the sides in the downwash from the rotors. Figure 38 shows examples of the ensemble-averaged unsteady pressures on the side of lander, showing the period content from rotor blade passage and wake interactions at five locations identified by yellow numbers in Figure 37. The largest interactions are the positive pressures for blade passage over the shoulder of the rotor arm at Locations 5 and 7. Location 4 between the rotors has smaller negative peaks, while Locations 8 and 16 do not show such a sharp response.

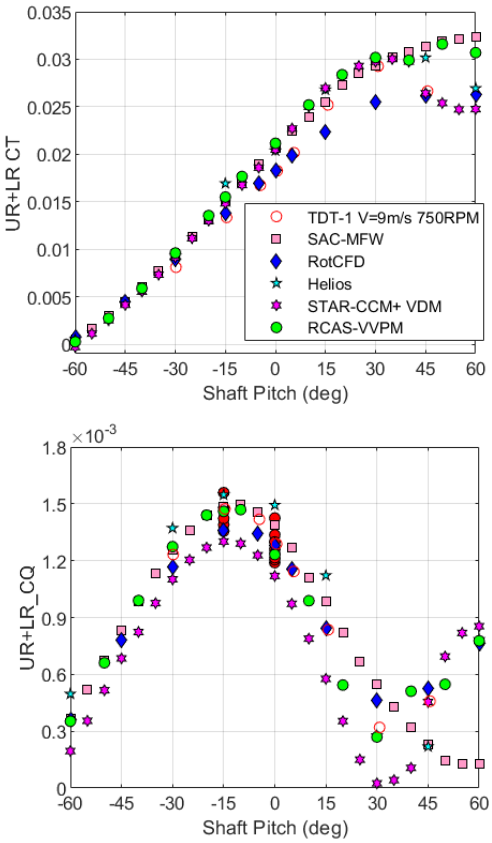


Figure 35. Cross-tool TDT-1 comparison for coaxial rotor pair thrust and torque at 750 rpm, V=9 m/s. (UR+LR = Upper rotor + Lower rotor)

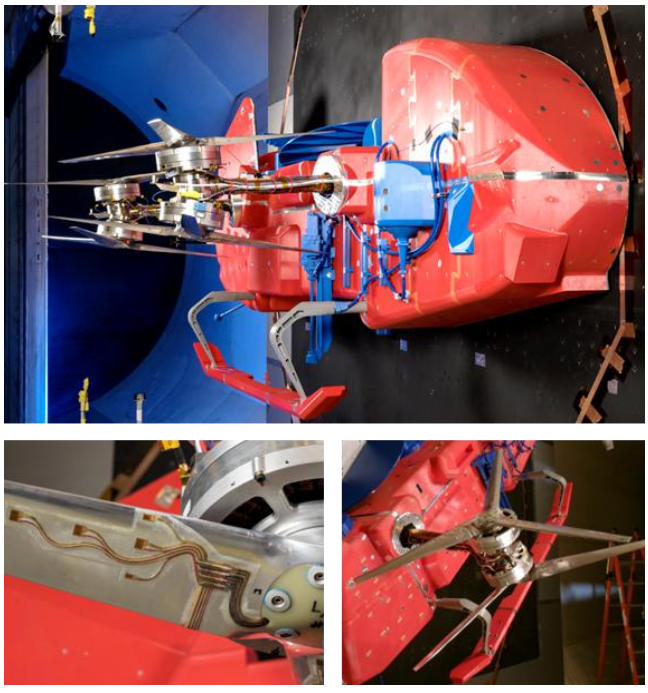


Figure 36. TDT-2A Half-Span, full-scale Dragonfly lander with Phase C Rotors in the TDT (2025).

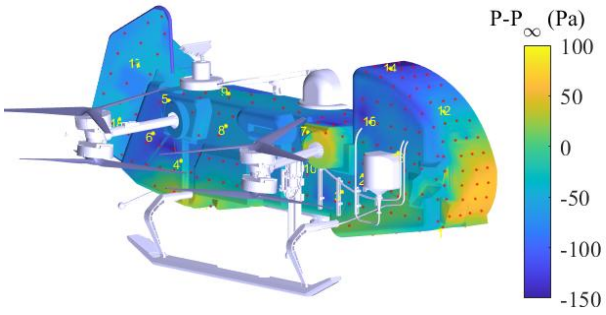


Figure 37. Example pressure distribution from the static pressure taps on the TDT-2A model, V~ 6m/s, pitch = 0°, all rotors at 1025 rpm.

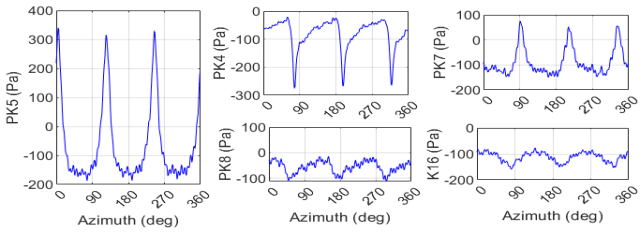


Figure 38. Example of unsteady pressure vs. rotor azimuth from the Kulites on the TDT-2A model. (V = 6 m/s, SA = 0°, all rotors at 1025 rpm)

Figure 39 shows an example of the time averaged thrust and torque coefficients for the forward stacked rotor pair over a model pitch range of ±45°, at V = 2.5 to 9.09 m/s, and 1025 rpm. This range covers descent, cruise, and climb conditions. The forward pair is most representative of an isolated rotor, since the aft pair experiences strong rotor and body aerodynamic interactions.

Figure 40 shows an example of the harmonic amplitude of rotating frame blade bending and fixed frame rotor loads. The blade normal bending is primarily 1p from forward flight, while the fixed frame loads are primarily 3p/6p/9p, with some 1p from rotor imbalance and dissimilarity. These results are currently being modeled using RCAS-VVPM and Helios.

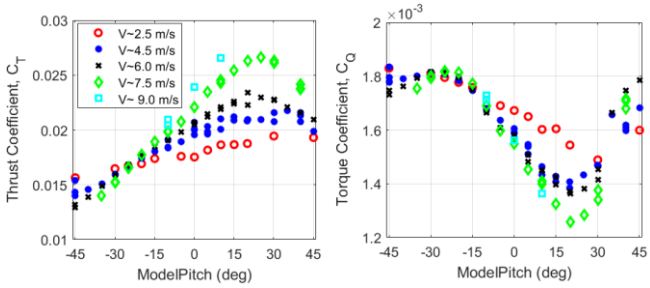


Figure 39. Example of thrust and torque coefficient vs pitch for TDT-2A forward stacked rotors at V = 2.5 to 9.09 m/s, with all rotors at 1025 rpm.

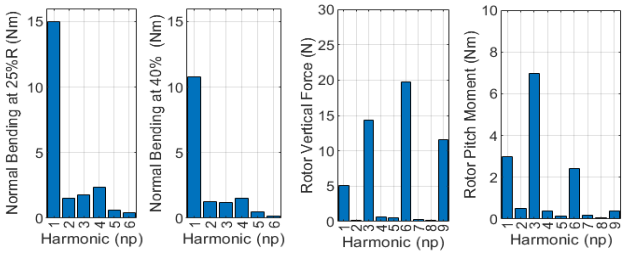


Figure 40. Example of blade bending and rotor harmonic amplitudes at V~6 m/s, α = 0°, 1025 rpm.

TDT-2A Aerodynamics Validation (2025-2026)

The rotor data gathered from the TDT-2A test were utilized to validate the CFD modeling approach used to simulate Titan flight. The bulk of the validation dataset utilized the same approach that the Titan database employs: STAR-CCM+ with RANS-VDM. All 791 unique heavy gas test points collected during the test campaign were simulated with this approach. Higher-fidelity spot checks using Helios were also simulated for select conditions.

The CFD setup matched tunnel conditions as closely as possible, utilizing tunnel geometry procured from a scan which included details of the inlet contraction, outlet expansion, and main tunnel section including slots into the plenum. Detailed CAD of the lander body was also supplemented with in-situ scans of the model which allowed for re-creating of installation effects including wiring harnessing. Model support struts and the splitter plate were also included.

Detailed scans of the blades also revealed slight deformations of the as-built blades compared to the design, with approximately 0.45 degrees more twist at the tip and slight flatwise deformation. The twist distribution utilized in the Virtual Disk modeling was updated to account for this, and a new blade was lofted for discrete blade CFD. Exact tunnel conditions were matched for each test point, including heavy gas properties based on measured purity ratios, tunnel speed, model orientation, and rotor RPMs.

Although the CFD solutions can be data-mined for various comparisons to test data including measured loads and surface pressures, as well as for detailed understanding of the flow in any given condition, the primary metrics of interest were rotor thrust and torque. Figure 41 and Figure 42 show parity plots of these loads in the shaft axis across all test conditions and colored by model pitch.

Overall RMSE values align with TDT-1 prediction errors, despite a more complex model with greater interactions. This attests that including many details of the complex test article into the CFD model is important. For *Dragonfly*, this has a profound impact on the model uncertainty provided to Mobility Closed-Loop Simulation (CLS), as this uncertainty practically has not grown between the TDT-1 and the more complex TDT-2A tests.

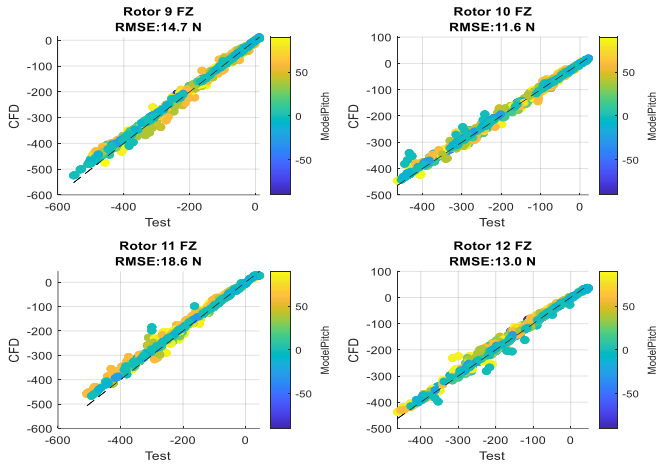


Figure 41. Parity Plots of Thrust for Each Rotor Comparing TDT-2A and CFD Data for all Conditions.

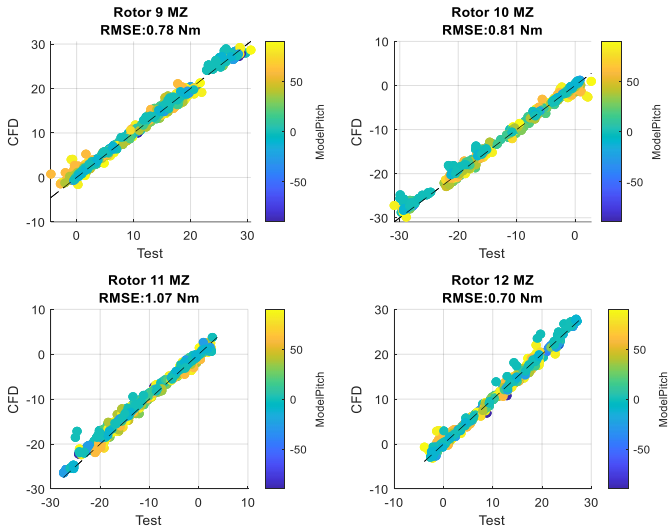


Figure 42. Parity Plots of Torque for Each Rotor Comparing TDT-2A and CFD Data for all Conditions.

Helios results for a nominal forward flight condition are shown in Figure 43 and show good agreement with both the test data and the mid-fidelity STAR-CCM+ Virtual Disk data.

While final analysis of the TDT-2A and TDT-2B datasets is still in progress (particularly for TDT-2B), the TDT-2A test, with sample data and validation comparisons shown in this paper, provided an invaluable opportunity to test flight-representative rotors in near-Titan conditions, validate the CFD modeling approach utilized to simulate flight on Titan, and define uncertainties to be carried out through downstream analysis that utilizes CFD simulations of flight on Titan.

At this stage, the three-bladed Phase C rotor is moving forward to final manufacturing for the *Dragonfly* lander. The TDT-1 test of an isolated Phase B* rotor pair, TDT-2A test of a full-scale semi-span *Dragonfly* lander model equipped with three-bladed Phase C rotors, and the recent TDT-2B test of a scaled full-span lander model with COTS rotors have provided unprecedented valuable validation data to verify the performance of the rotor design and the various computational tools at different institutions.

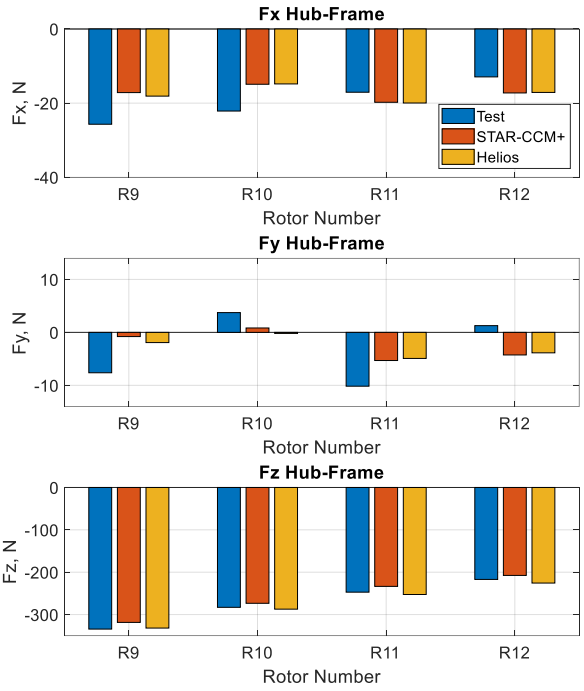


Figure 43. Rotor Shaft Forces for Nominal Forward Flight Condition at 6 m/s, -10 deg pitch, 1025 rpm, comparing Test, STAR-CCM+, and Helios results.

CONCLUSIONS

The present paper summarizes the rotor design and optimization efforts for the *Dragonfly* lander to be launched to Titan in 2028. The work presented was conducted over a period of almost ten years and includes an overview of feasible rotorcraft flight on Titan, conceptual studies on the multi-rotor configuration chosen for *Dragonfly*, and summarizes the various stages of conceptual, preliminary, and detailed design. As the first rotorcraft mission in the outer solar system, the various design constraints and requirements were not set from the beginning but instead evolved over the course of the project phases with other subsystems. In this sense, *Dragonfly* is truly a unique rotorcraft application, providing lander mobility to a NASA Science mission. As the rotor design and subsystems evolved, so did the computational tools and wind tunnel tests to provide confidence in the final rotors for *Dragonfly*.

A few key conclusions are provided below:

- Basic momentum theory and blade-element momentum theory provide a very good baseline design for a preliminary rotor planform (chord and twist).
- The airfoil choice for the *Dragonfly* rotors was driven primarily by considerations pertaining to Reynolds

scaling, roughness sensitivity, manufacturability, thick(er) airfoils, condensation, and stall behavior, while actual airfoil c_l/c_d was of secondary importance.

- The rotor planform converged to a simple tapered shape that provided ease in manufacturing and allowed smooth blending into the rotor hub, thus lowering hub parasite drag. It was also the planform that performed best over all relevant flight conditions of the *Dragonfly* lander.
- The legacy blade twist distribution balancing performance in hover and climb against cruise and, in particular, descent became an important design feature.
- The computational Virtual Disk Method in RotCFD and STAR-CCM+ became the keystone mid-fidelity method for rotor performance prediction and the aero database generation. Cross-validation between these tools was valuable throughout the verification and validation process of the rotor design.
- Comprehensive analysis (RCAS) was pivotal in quantifying rotor vibrations and laying out the structural design of the stiff rotor blades from Phase B to Phase B*.
- The TDT-1 test was instrumental in verifying performance of the design and validating the Virtual Disk Method tool for all aero performance table generation.
- A focused investigation of 12 variants to the Phase B* rotor resulted in the two-bladed Phase C rotor becoming the successor, with a net gain in range of several hundred meters.
- RCAS analyses of vibratory levels at specific instrument locations inside the lander ultimately pivoted transition to the three-bladed Phase C rotor with very similar performance due to keeping constant rotor solidity.
- Subsequent efforts focused on twist optimization of the three-bladed Phase C rotor did not result in appreciable gains. The blade planform was maintained also because tools were established and provided confidence to predict performance at Titan.
- The TDT-2A test confirmed performance of the three-bladed Phase C rotor without any appreciable change in total predictive uncertainty for *Dragonfly* flight on Titan.
- The systematic vetting of the *Dragonfly* rotor design through test and cross-validation of computational tools provided increased confidence in the rotor design.

Rotor design, optimization, testing, and manufacturing are now completed. *Dragonfly* is getting ready for flight.

Author contact: Sven Schmitz sus52@psu.edu
Kate Gruber katherine.a.l.gruber@lmco.com

ACKNOWLEDGMENTS

This work was funded by the NASA New Frontiers *Dragonfly* Mission. The Pennsylvania State University acknowledges financial support from the Johns Hopkins University Applied Physics Laboratory. Sikorsky's efforts were funded through Lockheed Martin Space, under contract from the Johns Hopkins University Applied Physics Laboratory as part of the *Dragonfly* Phase B and Phase C contract from NASA. The Pennsylvania State University authors also thank the NASA Advanced Supercomputing Division for their support in using the High-End Computing Capability Pleaides GPU nodes for this work. In addition, the authors thank Larry Young, Stephen Wright, and Carl Russell of the NASA Ames Research Center and Brian Wake of Sikorsky for valuable comments on the paper. Lastly, the authors would like to thank the staff of the NASA Langley 14- by 22-Foot Subsonic Wind Tunnel and Transonic Dynamics Tunnel, the staff of the NASA Ames National Full-Scale Aerodynamics Complex, and the larger *Dragonfly* test team for obtaining and post-processing the experimental data.

REFERENCES

1. Young, L. A., "Exploration of Titan Using Vertical Lift Aerial Vehicles," NASA Headquarters and Lunar and Planetary Institute Forum on Innovative Approaches to Outer Planetary Exploration, LPI Contribution # 1084, Houston, TX, February 21-22, 2001.
2. Lorenz, R. D., "Flexibility for Titan Exploration: The Titan Helicopter," NASA Headquarters and Lunar and Planetary Institute Forum on Innovative Approaches to Outer Planetary Exploration, LPI Contribution # 1084, Houston, TX, February 21-22, 2001.
3. Lorenz, R., Mitton, J., "Titan Unveiled," Princeton University Press, 2008.
4. Lorenz, R. D., Turtle, E. P., Barnes, J. W., Trainer, M. G., Adams, D. S., Hibbard, K. E., Sheldon, C. Z., Zacny, K., Peplowski, P. N., Lawrence, D. J., Ravine, M. A., McGee, T. G., Sotzen, K. S., MacKenzie, S. M., Langelaan, J. W., Schmitz, S., Wolfarth, L. S., and P. D. Bedini, "Dragonfly: a rotorcraft lander concept for scientific exploration at Titan," Johns Hopkins APL Technical Digest Vol. 34, No. 3, pp. 374-387, 2018. https://dragonfly.jhuapl.edu/News-and-Resources/docs/34_03-Lorenz.pdf
5. Moorman, R. W., "To the Heavens and Beyond," Vertiflite, November/December Issue, pp. 22-25, 2019.
6. Moorman, R. W., "Dragonfly Evolution," Vertiflite, November/December Issue, pp. 24-28, 2024.
7. Lorber, P., Wallace, B., Sharma, K., Bowles, P., Edquist, K., McGrath, B., Kellermeyer, W., Gilles, P., "Dragonfly Preparation for Powered Flight Wind Tunnel and CFD Modeling," Vertical Flight Society 81st Annual Forum

and Technology Display, Virginia Beach, VA, May 2025.

8. Langelaan, J., Schmitz, S., Palacios, J., Lorenz, R., "Energetics of rotary-wing exploration of Titan," IEEE Aerospace Conference, 2704, 2017. DOI: 10.1109/AERO.2017.7943650.

9. Langelaan, J., Schmitz, S., Adams, D., and Lorenz, R. D., "Conceptual Design of the Dragonfly Lander," Vertical Flight Society 77th Annual Forum Proceedings, Virtual, May 2021.

10. Cornelius J., Langelaan J., Opazo, T., Schmitz, S., Adams, D., Rodovskiy, L., Villac, B., Young, L., "Dragonfly – Aerodynamics during Transition to Powered Flight," Vertical Flight Society 77th Annual Forum Proceedings, Virtual, May 2021.

11. Robbins, M., Vaughan, R., Putnam, Z., McGee, T., "Rotorcraft Flight on Saturn's Largest Moon Titan: An Integrated Approach for Extraterrestrial Vertical Flight," AIAA SciTech Forum, Orlando, FL, Jan 2026. DOI: 10.2514/6.2026-2529.

12. Wright, M., Edquist, K., Vaughan, R., "EDL Concept of Operations for the Dragonfly Rotorcraft Mission to Titan," AIAA SciTech Forum, Orlando, FL, Jan 2026. DOI: 10.2514/6.2026-1953.

13. Gruber, K., Regan, M., Trubelja, K., Perrotta, G., Tang, E., Boss, C., Misiorowski, M., "Unveiling the Unsteadiness: Modeling Dragonfly's Descent With an Aerodynamic Trajectory Framework," AIAA SciTech Forum, Orlando, FL, Jan 2026. DOI: 10.2514/6.2026-0018.

14. Gruber, K., Klimchenko, V., Regan, M., Trubelja, K., Kim, J, Bowles, P. Misiorowski, M., Perrotta, G., "The Evolution of Dragonfly's Design Using CFD at Titan," Vertical Flight Society 81st Annual Forum, Virginia Beach, VA, USA, May 20-22, 2025.

15. Koning, W., Johnson, W., and Grip, H., "Improved Mars Helicopter Aerodynamic Rotor Model for Comprehensive Analyses," AIAA Journal, Vol. 57, No. 9, Sept. 2019. DOI: 10.2514/1.J058045.

16. Grip, H., Johnson, W., Malpica, C., Scharf, D., Mandicc, M., Young, L., Allan, B., Mettler, B., San Martin, M., Lam, J., "Modeling and Identification of Hover Flight Dynamics for NASA's Mars Helicopter," AIAA Journal of Guidance, Control, and Dynamics, Vol. 43, No. 2, Feb. 2020. DOI: 10.2514/1.G004228.

17. Balaram, J., Aung, M., Golombek, M. P., "The Ingenuity Helicopter on the Perseverance Rover," *Space Science Reviews,* Vol. 217, No. 56, 2021.

18. Escobar, D., Chopra, I., Datta, A., "High-Fidelity Aeromechanical Analysis of Coaxial Mars Helicopter," AIAA Journal of Aircraft, Vol. 58, No. 3, May 2021. DOI: 10.2514/1.C035895.

19. Wright, S., Koning, W., Perez Perez, N., Cummings, H., and Johnson, W., "Predicted Performance Effects of Blade Elasticity on Testing of Rotors for Mars," Presented at the VFS Autonomous VTOL Technical Meeting, Mesa, AZ, Jan. 24-26, 2023.

20. Ramasamy, M., Johnson, B., Leishman, J. G., "Toward Understanding the Aerodynamic Efficiency of a Hovering Rotor," AHS International Specialists Meeting, January 2007.

21. "OVERFLOW 2.3d, Overset Grid Computational Fluid Dynamics Flow Solver With Moving Body Capability (OVERFLOW)", NASA Software Catalog, 2023. https://software.nasa.gov/software/LAR-20095-1

22. Schmitz, S., Heisler, R., Cornelius, J., Allred, G., Palacios, J., Juliano, B., Perrotta, G., and Ruiz, F., "NASA Dragonfly Mission – Coaxial Rotor Test & CFD Prediction," Vertical Flight Society 81st Annual Forum Proceedings, Virginia Beach, VA May 2025.

23. Rajagopalan, G., Baskaran, V., Hollingsworth, A., Lestari, A., Garrick, D., Solis, E., and Hagerty, B., "RotCFD – A Tool for Aerodynamic Interference of Rotors: Validation and Capabilities," AHS Future Vertical Lift Aircraft Design Conference, San Francisco CA, January 2012.

24. Sukra Helitek, "RotCFD: Rotor Computational Fluid Dynamics Integrated Design Environment, Software Package, Ver. 0.9.15 Build 402", Ames, IA, 2020. http://sukra-helitek.com/

25. Conley, S., Russell C., Kallstrom K., Koning W., Romander E., "Comparing RotCFD Predictions of the Multirotor Test Bed with Experimental Results," Vertical Flight Society 76th Annual Forum, Oct. 2020. https://rotorcraft.arc.nasa.gov/Publications/files/1429_Conley_070720.pdf

26. Rajagopalan, G., Thistle, J., and Polzin, W., "The Potential of GPU Computing for Design in RotCFD," AHS Technical Meeting on Aeromechanics Design for Transformative Vertical Lift, San Francisco, CA, January 2018.

27. Marshall, M., McCann, B., Mari, M., Tang, E., Rodovsky, L., Superfin, E., Shapiro, B., Goulet, J., "Modeling and Flight Performance of NASA's Dragonfly Rotorcraft Lander," AIAA SciTech Forum, Orlando, FL, Jan 2026 DOI: 0.2514/6.2026-2534.

28. Perrotta, G., Misiorowski, M., "Surrogate Modeling of Aerodynamic Loads on the Dragonfly Lander in Flight," AIAA SciTech Forum, Orlando, FL, Jan 2026. DOI: 10.2514/6.2026-2530.

29. U.S Army Combat Capabilities Development Command Aviation & Missile Center, "HELIOS User's Guide v12.3," Moffett Field, CA: 2023.

30. U.S. Army Combat Capabilities Development Command Aviation & Missile Center, “RCAS Theory Manual,” Moffett Field, CA: August 2021.

31. He, C., and Zhao, J., “Modeling Rotor Wake Dynamics with Viscous Vortex Particle Method,” AIAA Journal, Vol. 47, No. 4, April 2009. DOI: 10.2514/1.36466.

32. Cornelius, J. K., Kinzel, M. P., Schmitz, S., “An Efficient CFD Approach for Coaxial Rotor Simulations in Hover,” AIAA Journal of Aircraft, Vol. 58, No. 1, pp. 197-202, 2020. DOI 10.2514/1.C036037.

33. Lorenz, R. D., Schmitz, S., Kinzel, M., “Prediction of Aerodynamically-Triggered Condensation: Application to the Dragonfly Rotorcraft in Titan's Atmosphere,” Aerospace Science and Technology, Vol. 114, July 2021. DOI: 10.1016/j.ast.2021.106738.

34. Hoffmann, M. J., Reuss Ramsay, R., and Gregorek, G. M., “Effects of Grit Roughness and Pitch Oscillations on the NACA 4415 Airfoil,” NREL/TP-442-7815, 1996.

35. Allred, G. H., “Mission-Driven Rotor Conceptual Design for Future Multi-Rotor Vehicles – Application to NASA Dragonfly,” M.S. Thesis, The Pennsylvania State University, 2024.

36. Chattot. J. J., “Optimization of Propellers Using Helicoidal Vortex Method,” in Numerical Simulations of Incompressible Flows, pp. 375-384 (2003). DOI: 10.1142/9789812796837_0022.

37. Cornelius, J. K., and Schmitz, S., “Dragonfly Rotor Optimization Using Machine Learning Applied to an OVERFLOW-Generated Airfoil Database,” Journal of the American Helicopter Society, Vol. 71, (1), 2026, DOI: 10.4050/JAHS.71.022001.

38. Cornelius, J and Schmitz, S., “Rotor Performance Predictions for UAM - Single vs Coaxial Rigid Rotors,” Vertical Flight Society Aeromechanics for Advanced Vertical Flight, 2022.

39. Asiatico, J., Mitchell, B., Miles, Z., and Kinzel, M. P., “An Evaluation of Uncertainty for the Dragonfly Aircraft in the 14-By-22 Foot Subsonic Wind Tunnel,” AIAA Aviation Forum and Ascend, Las Vegas, NV, July-Aug. 2024. DOI: 10.2514/6.2024-4057.

40. Dellinger, W., Edquist, K., and Young, L., “Dragonfly Model Tested in NFAC,” Vertiflite, July/August Issue, pp. 48-49, 2024.

41. Coleman, D. G., Sharma, K. J., Bowles, P. O., Lorber, P. F., and Perrotta, G. M., “Dragonfly CFD Validation and Uncertainty Quantification,” Aviation Forum and Ascend, Las Vegas, NV, July 2025. DOI: 10.2514/6.2025-3314.

42. Newton, L., Vignali, M., Nieves Lugo, D., and Kinzel, M., “Aerodynamics of NASA’s Dragonfly Lander: An Assessment of Adverse Yaw Due to Rotor-Body Interactions,” American Astronomical Society Meeting Abstracts, Vol. 57, (2), January 2025.

43. Ventura Diaz, P., Yoon, S., Edquist, K., “High-Fidelity Computational Modeling of Dragonfly Lander during Preparation for Powered Flight,” VFS Forum 81 Annual National Forum, May 2025.

44. Ventura-Diaz, P., Yoon, S., and Edquist, K. T. "High-Fidelity Simulations of a Dragonfly Lander Test Article in the National Full-Scale Aerodynamics Complex," Aviation Forum and Ascend, Las Vegas, NV, July 2025. DOI: 10.2514/6.2025-3665.

45. Zucker, C., Farrell, W., Amaya, L., McGee, T. G., Shapiro, B., N., Asiatico, J., and Kinzel, M. P., “An assessment of Dragonfly-Backshell aerodynamics preparing for the initial flight on Titan,” Acta Astronautica, Vol. 224, pp. 127-137, 2024, DOI: 10.1016/j.actaastro.2024.07.046.

46. Corliss, J., and Cole, S., “Heavy Gas Conversion of the NASA Langley Transonic Dynamics Tunnel,” AIAA Paper 1998-2710, 20th AIAA Advanced Measurement and Ground Testing Technology Conference, Albuquerque, NM, June 1998.

47. Ivanco, T., Piatak, D., Sekula, M., Simmons, S., Babel, W., Collins, J., “A New High Channel-Count, High Scan-Rate, Data Acquisition System for the NASA Langley Transonic Dynamics Tunnel,” AIAA 2016-1149, 54th AIAA Aerospace Sciences Meeting, San Diego, CA, Jan 2016. DOI: 10.2514/6.2016-1149.